Microstructure and mechanical properties of gas metal arc welded CoCrFeMnNi joints using a 410 stainless steel filler metal

Jiajia Shen [a,*], Rita Gonçalves [a], Yeon Taek Choi [b], J.G. Lopes [a], Jin Yang [c], N. Schell [d], Hyoung Seop Kim [b], J.P. Oliveira [a,e,**]

[a] UNIDEMI, Department of Mechanical and Industrial Engineering, NOVA School of Science and Technology, Universidade NOVA de Lisboa, 2829-516, Caparica, Portugal
[b] Graduate Institute of Ferrous Technology, POSTECH (Pohang University of Science and Technology), Pohang, 790-794, South Korea
[c] School of Materials Engineering, Shanghai University of Engineering Science, Shanghai, 201620, China
[d] Helmholtz-Zentrum Hereon, Institute of Materials Physics, Max-Planck-Str. 1, Geesthacht, 21502, Germany
[e] CENIMAT|i3N, Department of Materials Science, School of Science and Technology, NOVA University Lisbon, Caparica, Portugal

A R T I C L E   I N F O

A B S T R A C T

The use of filler materials during fusion-based welding processes is widely used to regulate and modify the composition of the welded joints aiming at producing a desired microstructure and/or achieving an improvement in its mechanical performance. Welding of high entropy alloys is still a new topic and the impact of different filler materials on the microstructure and mechanical properties is yet unknown. In this work, gas metal arc welding of the CoCrFeMnNi high entropy alloy using 410 stainless steel as a filler wire was performed. The microstructural evolution of the welded joints was evaluated by optical microscopy, scanning electron microscopy aided by electron backscattered diffraction, high energy synchrotron X-ray diffraction and thermodynamic calculations. Meanwhile, the mechanical behavior of the welded joint, as well as the local mechanical response were investigated with microhardness mapping measurements and with non-contact digital image correlation during tensile loading to failure. The weld thermal cycle promoted solid state reactions in the heat affected zone (recovery, recrystallization and grain growth), which impacted the microhardness across the joint. The role of the 410 stainless steel filler material in the solidification path experienced by the fusion zone was evaluated using Scheil-Gulliver calculations, and a good agreement with the experimentally observed phases was observed. Despite the addition of the 410 stainless steel filler was not conducive to an increase in the fusion zone hardness, the associated bead reinforcement promoted an improvement in both the yield and tensile strengths of the joint compared to a similar weld obtained without filler material (355 vs 284 MPa and 641 vs 519 MPa, respectively). This allows to infer that the addition of filler materials for welding high entropy alloys is a viable method for the widespread use of these novel materials. In this work, by coupling microstructure and mechanical property characterization, a correlation between the processing conditions, microstructure and mechanical properties was obtained providing a wider basis for promoting the application of gas metal arc welding of high entropy alloys for industrial applications.

1. Introduction

The concept of high entropy alloys was first introduced in 2004 [1,2] and these materials were initially defined as alloys composed by at least five elements, each with a composition ranging from 5 to 35 at. %. Another widely used term that encompasses these materials is multi-principal element alloys. High entropy alloys break the traditional concept of single principal component design of alloys, and this new design strategy can produce four core effects, namely high entropy effect, slow diffusion effect, severe lattice distortion effect and cocktail effect [2,3]. All of these are known to make these novel materials exhibit potential advantages over conventional metallic materials in terms of strength [4], hardness [5], fracture toughness [6], and corrosion resistance [7]. Among the wide number of compositions available, the most

---

studied alloy is the equiatomic CoCrFeMnNi which possesses a single phase FCC structure and remarkable mechanical properties [8]. Such properties make these materials as promising candidates to be used as structural components in various engineering applications.

Welding, as a key manufacturing technology, is widely used in the energy, aerospace, and shipbuilding industries. Owing to the potential interest on the use of high entropy alloys as structural materials in these industries, it is fundamental to conduct weldability studies to ensure the potential applicability of these emerging materials [9].

Currently, weldability studies focused on CoCrFeMnNi high entropy alloys is expanding, mainly focusing on gas tungsten arc welding [10], laser beam welding [11–13], electron beam welding [10,14] and friction stir welding [15–17]. Recently, Lin et al. [18] joined the CoCrFeMnNi high entropy alloy by ultrasonic welding, obtaining a sound joint with no defects or detrimental phases. Overall, the CoCrFeMnNi alloy exhibits good weldability under different welding methods when similar joining is attempted. To expand the range of industrial applications for CoCrFeMnNi high entropy alloys, meeting the needs for dissimilar welded structures, such as in those found in nuclear reactors and in high temperature components, researchers started to turn their attention to the dissimilar welding (when two different base materials or the addition of filler wire is attempted) involving the CoCrFeMnNi alloy [19–27]. The main challenge during dissimilar welding is the need to control and/or adjust the chemical composition of the fusion zone so that its microstructure and mechanical properties are suitable for the targeted applications. However, the mixing of two materials with different compositions, combined with the weld thermal cycle, can promote the formation of undesirable phases and/or intermetallic compounds. Therefore, it is critical to have a systematic understanding of the evolution of the microstructure and mechanical properties of dissimilar joints involving high entropy alloys.

Regarding this topic, the existing literature details works on dissimilar welding of the CoCrFeMnNi high entropy alloy to both 316 stainless steel [28,29] and duplex stainless steel [30] using fusion-based methods, while dissimilar joining of CoCrFeMnNi to 304 stainless steel by friction stir welding was also accomplished [31]. Recently, Nam et al. [24] used 308L stainless steel and CoCrFeMnNi high entropy alloy as filler materials to weld an as-cast CoCrFeMnNi alloy, and the mechanical properties (yield strength, maximum tensile strength and elongation) obtained were slight superior to those of the original base material. Afterwards, they used the same filler wire to weld as-rolled CoCrFeMnNi high entropy alloys [26], but now a decrease in the tensile properties was observed. The same group then welded 304 stainless steel using CoCrFeMnNi high entropy alloy as a filler material [22]. Moreover, a CuCrFeMnNi filler wire was used to join a rolled CoCrFeMnNi [32], while a Cu-coated CoCrFeMnNi filler wire was seen to increase the mechanical performance of the joint [32]. The above studies all have reported obtaining sound dissimilar welded joints, however, research around this theme is still scarce, especially given the large number of filler materials that exist.

In the present work, ER410-NiMo stainless steel was selected as a filler wire for joining a CoCrFeMnNi high entropy alloy by gas metal arc welding. The microstructural evolution of the welded joints was evaluated by optical microscopy, scanning electron microscopy aided by electron backscattered diffraction, high energy synchrotron X-ray diffraction and thermodynamic calculations. Mechanical property analysis was performed via microhardness mapping, as well as tensile testing aided by digital image correlation. A correlation between the weld thermal cycle, microstructure evolution and resulting mechanical properties is established towards the implementation of these materials and welding process in structural applications.

2. Experimental procedure

2.1. Materials

In this work, an equiatomic CoCrFeMnNi high entropy alloy with a thickness of 3 mm was prepared by vacuum induced melting as described in [28]. Following cold rolling at room temperature, a thickness of 1.5 mm was obtained. Before welding, the as-rolled material was cut into 60 × 60 mm squares for butt joining. The faying edges were polished and cleaned with acetone and alcohol to remove any contaminants that could be harmful to the welded joint.

2.2. Gas metal arc welding procedure

Previous work on autogenous welding of this CoCrFeMnNi material revealed good material weldability [33]. To evaluate if the addition of a filler material has a positive effect on the mechanical response of the CoCrFeMnNi alloy joints, gas metal arc welding using a 410 martensitic stainless steel filler was used. The process is schematically detailed in Fig. 1. For reference, the compositions of the two materials used, base and filler material, are detailed in Table 1.

To prevent oxidation of the fusion and heat affected zones during welding, Ar was used on the top and bottom surfaces of the specimens as shielding gas. The selected welding parameters are detailed in Table 2. These parameters ensured full penetration welds with no evident defects.

After welding, electrical discharge machining (EDM) was used to obtain samples for microstructure and mechanical characterization. The dimensions of the samples used for mechanical characterization are detailed in Fig. 2.

2.3. Microstructure characterization

The welded specimens were first placed in epoxy resin, then ground with 400, 600, 1200, 2500 and 4000-grit SiC papers, and finally with a 3.0 μm diamond polishing paste until a mirror-like surface was obtained. To reveal the joint microstructure, the polished specimens were immersed in a solution of aqua regia (5 ml HNO_3 and 15 ml HCl) at room temperature. Due to the different corrosion behavior of the welded joint, the etching time was found to be around 90–110 s for the base material (BM) and heat affected zone (HAZ), and approximately 190–220 s for the fusion zone (FZ). To observe the microstructure of the welded joints, light optical microscopy and scanning electron microscopy (SEM) coupled with both energy dispersive spectroscopy (EDS) and electron backscatter diffraction (EBSD) were used. For light optical microscopy, a Leica DMI 5000 M inverted optical microscope was used, while for SEM/EDS/EBSD, a JSM-7100F and a Helios Hikari UMSII were used. The TSL OIM Analysis 7.0 software was used to process the raw EBSD data.

To further investigate the role of the weld thermal cycle and addition of the ER410-NiMo filler on the welded joints, synchrotron X-ray diffraction was used. The synchrotron radiation experiments were done at the P07 High Energy Materials Science beamline at Petra III/DESY. A high photon energy of 87.1 KeV, corresponding to a wavelength of 0.14235 Å, was used. This photon energy allowed to perform diffraction experiments in transmission mode, enabling the determination of bulk microstructure information [34]. A beam with a size of 200×200 μm^2 starts to scan the welded joint in the base material, passes through the heat affected zone and fusion zone and finally finishes on the opposite side of the base material. A PerkinElmer 2D detector was used to capture the diffraction data. Standard LaB_6 powder was used for the calibration of the instrumental parameters using Fit2D software [35]. The sample-to-detector distance was determined to be 1335 mm. In addition, the synchrotron X-ray data were post-processed with a combination of GSASII [36] and MAUD [37], for single-peak fitting and Rietveld refinement, respectively. The experimental setup for the synchrotron X-ray diffraction measurements is schematically detailed in Fig. 3.
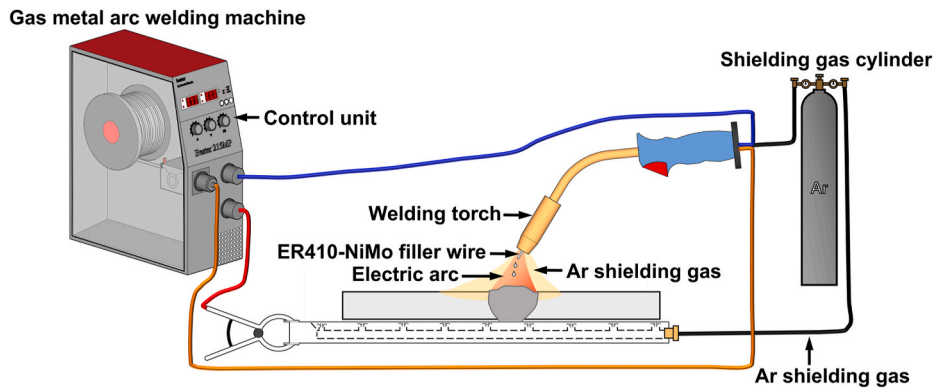
Fig. 1. Schematic of the gas metal arc welding set-up used in this work.

Table 1
Chemical composition of the base material and ER410-NiMo wire electrode (at. %/wt. %).

	Co	Cr	Mn	Ni	C	Si	Mo	Fe
Base material	20/21	20/18.53	20/19.6	20/21.01	–/–	–/–	–/–	20.0/19.9
Filler material	–/–	14.3/13.5	0.6/0.6	4.2/4.5	0.2/0.05	1.2/0.6	0.29/0.5	Balance

Table 2
Gas metal arc welding parameters used in this work.

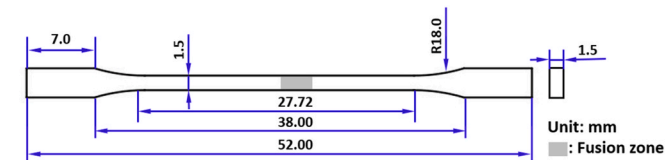| Voltage	Torch travel speed	Wire feed speed	Shielding gas	Gas flow rate
V	mm/min	mm/min		L/min
15.4	230	2000	Ar	16

Fig. 2. Geometry and dimensions of specimens used for uniaxial tensile testing.

2.4. Thermodynamic calculations

The Scheil-Guliver model, available in ThermoCalc, was used as a thermodynamic calculation tool to predict the non-equilibrium solidification path and phase structure evolution in the FZ of the welded joints. Here, it should be mentioned that the effect of the filler wire on the potential compositional heterogeneity of fusion-based welded joints (i.e., mixing ratio of base material and filler wire) is considered by performing the Scheil-Gulliver calculations with 10% dilution steps. During non-equilibrium thermodynamic calculations using the Scheil-Guliver model, certain elements can be set as fast diffusers, as these can greatly influence the solidification path experienced by the material. For steels and related alloys, carbon is usually set as fast diffuser [38]. Here, calculations were made with and without carbon selected as a fast diffuser. Although the CoCrFeMnNi alloy does not possess any carbon, upon melting of the 410 stainless steel filler material, there will be carbon incorporation by the fusion zone, which can then influence the microstructure evolution. The TCHEA5.1 database of ThermoCalc was used for these calculations.

2.5. Microhardness mapping and mechanical testing

Microhardness measurements and uniaxial tensile testing were used to study the mechanical properties of the joints. Vickers microhardness mapping was performed along the cross section of the welded joint on a Mitutoyo HM-112 hardness testing machine. A load of 0.5 kg was used with an indentation time of 10 s. The space between successive indentations in both transverse and longitudinal directions was 200 μm. Uniaxial tensile testing was performed on a Shimadzu tensile machine equipped with a 50 kN load cell. Tensile tests were conducted at room temperature at a tensile rate of 1×10^{-3} s. The loading direction was perpendicular to the welding direction. Three specimens were tested to determine the variability in mechanical properties of the joints. Moreover, digital image correlation (DIC) was applied to investigate the local
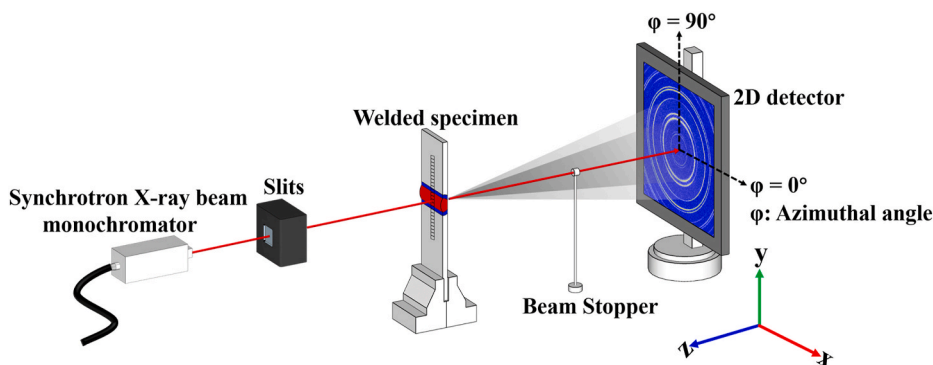

Fig. 3. Synchrotron X-ray diffraction set-up (not to scale).

deformation response of different regions in the welded joint (namely BM, HAZ and FZ). Here, it is worth mention that the welded specimens were not ground to remove the excess material on the fusion zone face and root upon the addition of the filler material. Moreover, prior to tensile testing the cutting surfaces were polished to remove the surface affected by the EDM process. After tensile testing, a Hitachi SU3800 SEM was used to observe the joint fracture surfaces.

3. Results and discussion

3.1. Microstructure evolution

Fig. 4 a) details a macroscopic overview of the cross-section of the gas metal arc welded joint. No welding defects are observed. Fig. 4 b), c) and d) detail the light optical microscopy images of the BM, HAZ and FZ, respectively. The fusion boundaries, marked with white dashed lines in Fig. 4, delimitate the FZ. As typically for welded joints obtained with filler material, there is the formation of a reinforcement on the face and root of the weld, as marked in Fig. 4 a), owing to the extra material coming from the filler wire. The face reinforcement is formed upon the addition of the molten filler wire and protrudes slightly as the wire moves forward during welding. The root reinforcement on the bottom surface of the joint is more obvious due to the surface tension of the melted wire during solidification [39]. From Fig. 4 b), c) and d), it can be broadly seen the evolution of the grain size and microstructure across

the welded joint. The BM region (Fig. 4 b)) has the smallest grain size due to the cold rolling imposed prior to welding. The grain size increases when entering in the HAZ (Fig. 4 c)). Before reaching the FZ boundary, within the partially melted zone, there is evidence of partial liquation of the existing grains (refer to Fig. 4 d)). At the HAZ/FZ interface, a typical solidification structure composed by dendrites is observed. Within the center of the FZ (Fig. 4 e)), coarse columnar grains grew owing to the highly directional solidification conditions experienced.

To further evaluate the microstructure evolution, EBSD was used. The EBSD map of the welded joint is depicted in Fig. 5. Due to the large size of the as-welded sample, the as-rolled CoCrFeMnNi BM is not included in the EBSD map shown in Fig. 5. At this instance, focus is mainly given to the HAZ and FZ regions, since the as-rolled BM was already significantly studied in the literature [29,33]. In Fig. 5, the white dashed lines represent the HAZ/FZ interface.

Combined with the macroscopic overview of the welded joint previously shown in Fig. 4, it can be clearly seen that there are no macroscopic defects such as porosity or cracks, indicating that a reliable metallurgical mixing between the CoCrFeMnNi alloy and the ERNiMo-410 stainless steel occurred. This also confirms that the selected welding parameters enabled to obtain a full penetration and defect-free joint.

The grain size evolution across the joint reproduces the impact of the weld thermal cycle on the recrystallization and growth behaviors, as it will be shown when a more detailed analysis of each region of the joint is presented. For now, and only considering the EBSD map of Fig. 5, it can
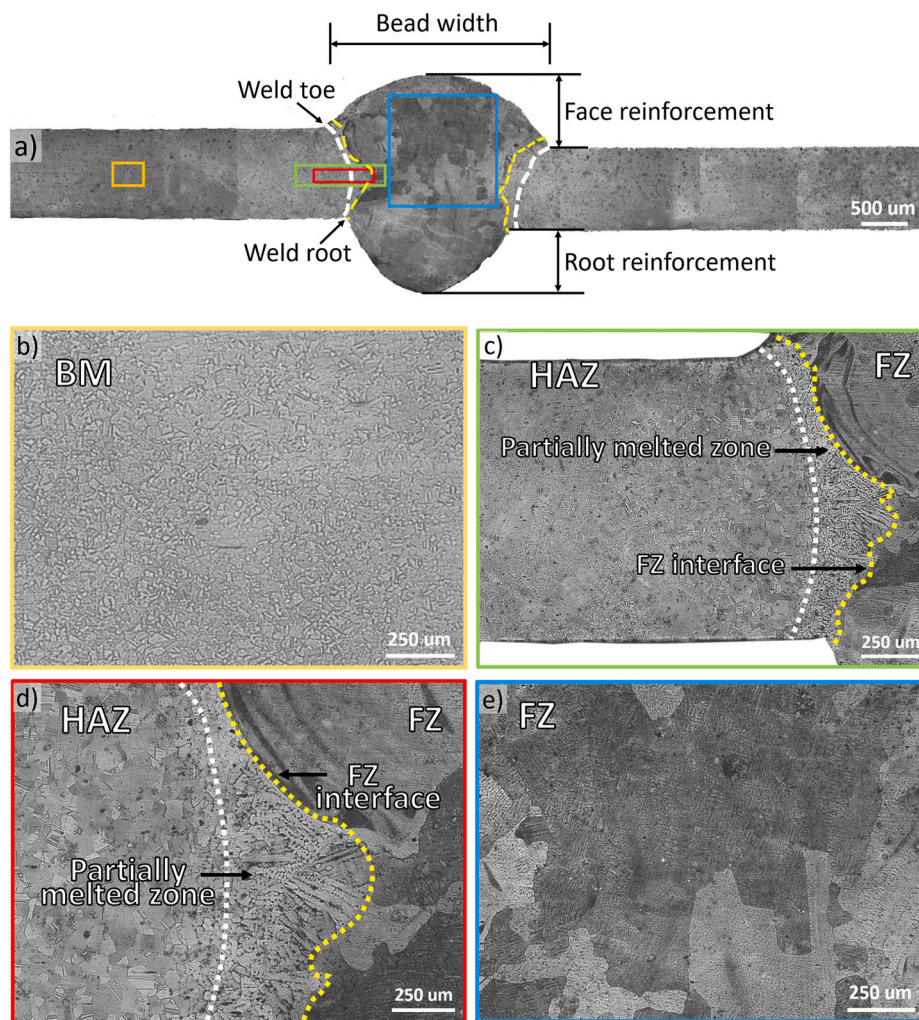

Fig. 4. Light optical microscopy of the gas metal arc welded CoCrFeMnNi joint obtained with ERNiMo-410 filler wire: a) overview of the cross-section of the welded joint; b) BM; c) HAZ and HAZ/FZ boundary; d) magnified HAZ and HAZ/FZ interface; e) FZ.
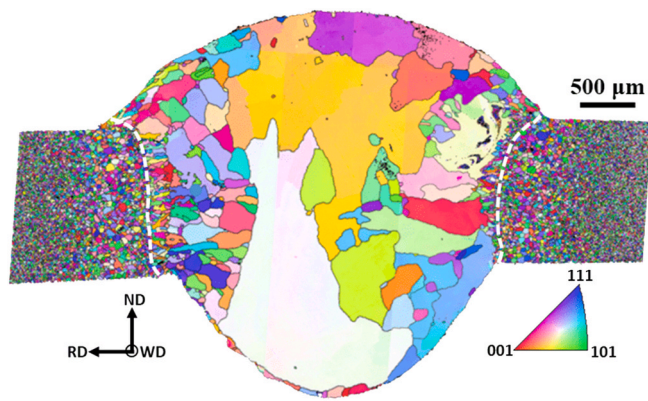
Fig. 5. EBSD map of the gas metal arc welded CoCrFeMnNi high entropy alloy with ERNiMo-410 filler wire.

Fig. 6. EBSD maps of the as-rolled CoCrFeMnNi BM: a) IPF map; b) KAM map.

be observed that the grain size increases towards the HAZ/FZ interface, which is due to the increased local peak temperature and permanence time at high temperatures. The higher the temperature and/or the permanence time at critical temperatures, the easier is the growth of the previously recrystallized grains.

At the edge of the fusion zone, the grain structure is significantly refined due to the presence of the cold heat affected zone. However, moving away from the HAZ/FZ boundary towards the weld centerline, there is a reduction of the thermal gradient while the temperature experienced by the material is higher which enabled to the development of large columnar grains. It should also be mentioned that the evolution and growth of these grains is also dependent on competitive growth mechanisms experienced by the material, where grains more favorably oriented will have their growth facilitated. These microstructure observations of the HAZ and FZ regions are in good agreement with the light optical micrographs previously shown in Fig. 4 c).

For further visualization and analysis of the microstructural features in different regions of the welded joint, attention is now given to representative EBSD maps obtained in four distinct regions: BM, HAZ near the BM, HAZ near the FZ and HAZ/FZ interface.

Fig. 6 a) and b) details the Inverse Pole Figure (IPF) and the Kernel Average Misorientation (KAM) maps for the as-rolled CoCrFeMnNi BM. As observed in Fig. 6 a), the grains are elongated along the rolling direction (RD), forming a refined, pancake-like grain structure with a width of about 2 μm. This grain morphology is common in rolled CoCrFeMnNi high entropy alloys [33]. In addition, considering the IPF map of Fig. 6, it is evident that the rolled base material is primarily oriented along the (1 1 1) direction. This is due to the fact that the (1 1 1) plane is the main slip plane for FCC materials. When the material is plastically deformed, dislocations tend to pile up along the primary slip system, forming slip bands parallel to the (1 1 1) close-packed plane [40, 41].

KAM maps detail the local misorientation of grains within the surrounding microstructure with point-to-point measurements. This can be used to evaluate the relationship between plastic deformation and microstructural misorientation. High KAM values usually correlate with high a dislocation density and/or with a region with high local strain. It can be seen from Fig. 6 b) that the KAM values preferentially lie between 4 and 5° (red color) in most areas of the base material (61.4%), implying a high dislocation density, which is associated to the large plastic deformation imposed during cold rolling of the CoCrFeMnNi high entropy alloy.

When entering in the HAZ, microstructural changes induced by the weld thermal cycle start to be clearly noticed. Fig. 7 a) details the IPF EBSD map obtained in the HAZ near the BM region, which corresponds to the low temperature HAZ region, i.e., further away from the weld centerline. The pancaked-shaped and highly deformed grains that previously existed are replaced by equiaxed ones, which is typical of
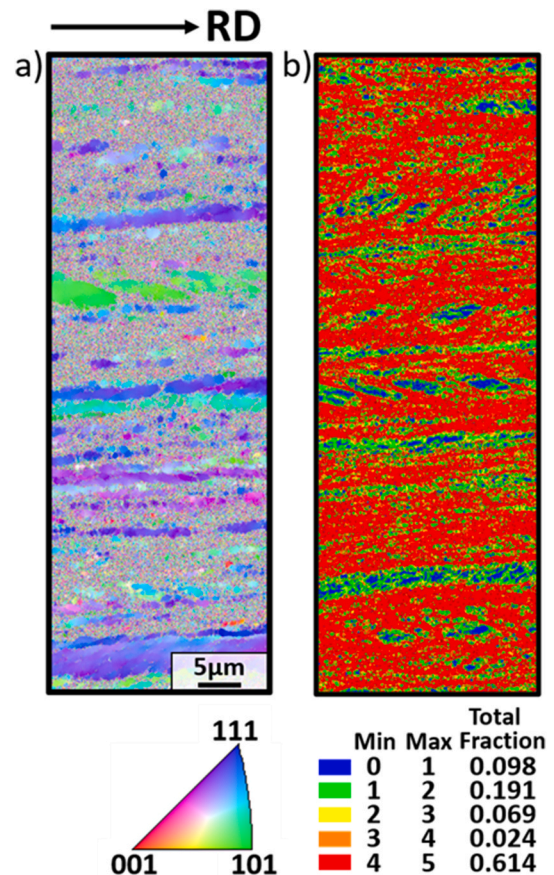
recrystallized microstructures. The BM in the rolled condition possesses a large amount of stored strain energy due to the previously imposed plastic deformation. Owing to the relatively low temperature experienced by the HAZ near the BM region during welding, grains will experience recovery, recrystallization and (eventually) minor grain growth. As a result, aside from evolving into an equiaxed morphology, there was also a minor increase of the grain size in this region, growing from ≈2.0 μm (in the BM) to ≈ 8.5 μm. It should be mentioned here that the main driving forces for recrystallization and grain growth are related to the process heat input, but also with the stored strain energy in the material. Comparing the distribution of the KAM values in the BM and HAZ near the BM regions, corresponding to Fig. 6 b) and Fig. 7 b), respectively, it can be found that the strain energy stored in the grains within the HAZ near the BM is significantly reduced compared to the BM. This can be attributed to the low temperature annealing-like treatment produced in this region during welding. This relatively low temperature cycle is usually associated with stress relaxation and can lead to grain growth, if higher temperatures and/or permanence times are imposed on the material [42]. In other words, the release of the previously stored strain energy contributes to the development of solid state transformations triggered by the weld thermal cycle. These solid state transformations include recovery, recrystallization and minor grain growth, which then translates into reduced dislocation density.

Fig. 7 c) details the EBSD phase map in the HAZ near the BM region. This region consists primarily of FCC phase and a small amount (≈2.7%) of BCC phase. As it will be shown after, when combining both EDS and synchrotron X-ray diffraction data (Figs. 11 and 12, respectively), this BCC phase can be assigned to the presence of Cr–Mn-based oxides.

The presence of a large number of annealing twins was detected in the HAZ near the BM region, with multiple ∑3 twin boundaries being observed, as identified by the red solid lines of Fig. 7 d). The driving

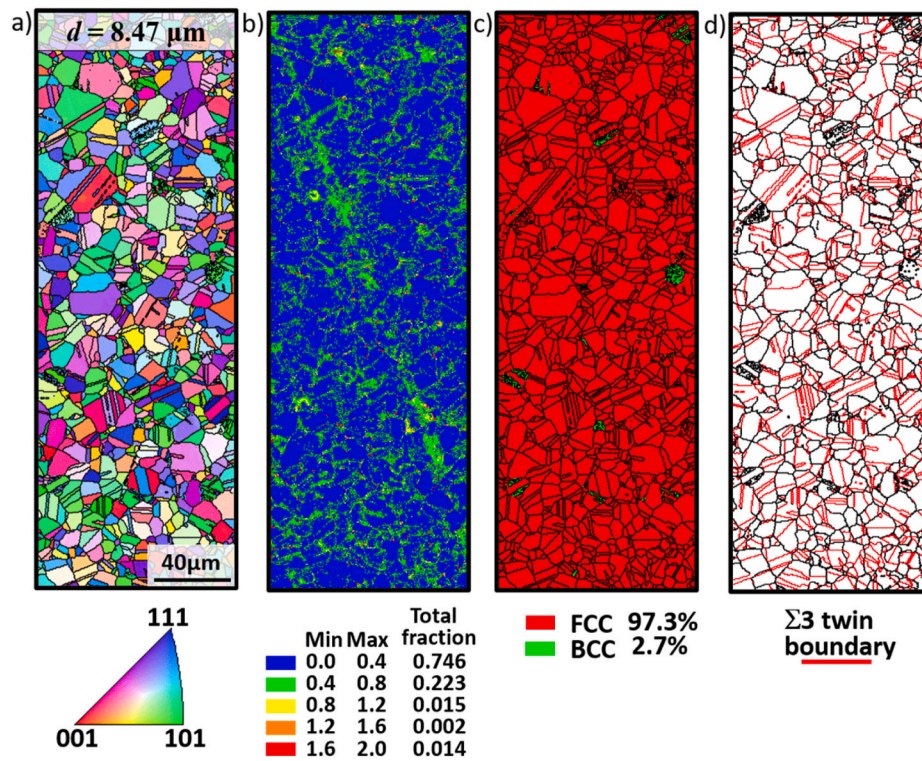**Fig. 7.** EBSD maps of the HAZ near the BM region: a) IPF map; b) KAM map; c) Phase diagram; d)∑3 twin boundaries map.

force for the formation of these ∑3 twins is the high strain energy (dislocation density) stored in the material and sufficiently high temperature. Generally, annealing twins are produced in recrystallized grains, and their density is proportional to the twin boundary fraction. From the ∑3 twin boundary map shown in Fig. 7 d), the fraction of ∑3 twins is approximately ≈40.5%, uncovering that the weld thermal cycle,

with a low peak welding temperature in the HAZ near the BM region, can induce the formation these ∑3 twins in the previously cold worked material.

Attention is now given to the HAZ near the FZ region. Fig. 8 details the EBSD maps at this location, which correspond to the high temperature HAZ region. Here, the grains become significantly coarser
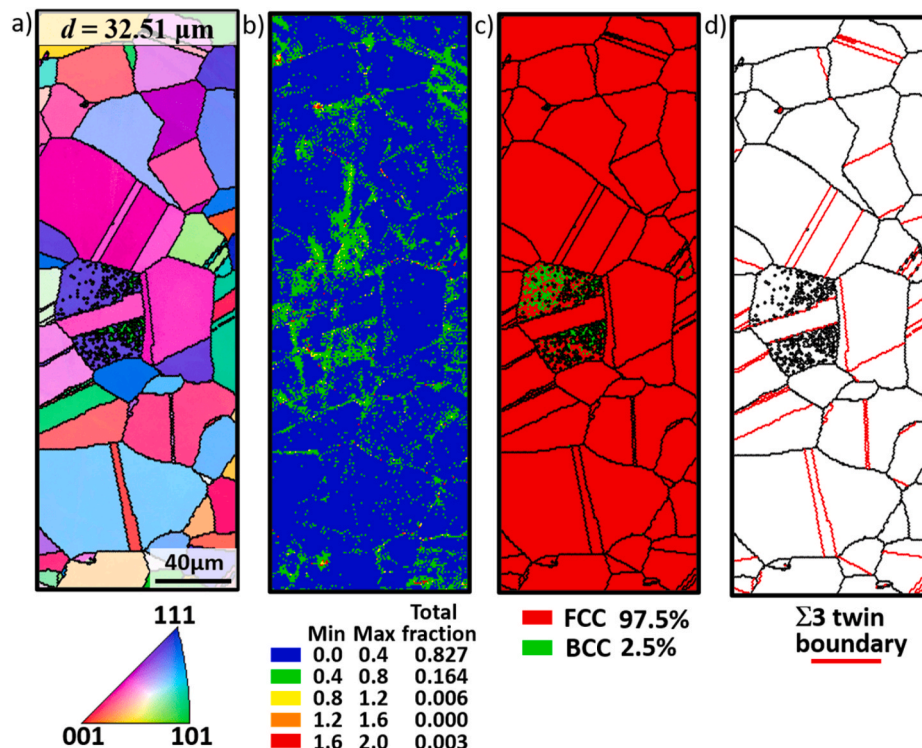

Fig. 8. EBSD maps of the HAZ near the FZ region: a) IPF map; b) KAM map; c) phase diagram map; d)∑3 twin boundaries map.

increasing from ≈8.5 μm, in the low temperature HAZ, to ≈32.5 μm (refer to Fig. 7 a) and Fig. 8 a), respectively). This significant increase indicates a dominance of a grain growth mechanism over recrystallization. Solid state phenomena such as those observed in this work, i.e., recovery, recrystallization and grain growth, are intimately related to the starting material condition and distance to the welding heat source. Specifically, regarding the HAZ near the BM and the HAZ near the FZ regions, the former experienced a lower peak temperature than the latter, which would be similar to a short low-temperature annealing, in which recrystallization and minor grain growth occurred. However, for the HAZ near the FZ region, there is evidence of significant grain growth, since higher peak temperatures are experienced at this location. This would resemble the effect of a short and high temperature heat treatment where grain growth is favored.

The essence of grain growth is the migration of grain boundaries in the material, which promotes mutual engulfment and subsequent growth of preexisting grains. The main driving forces for this process originate from the difference in the energy stored in adjacent grains or in the decrease of the grain interfacial energy, i. e., as the grain growth behavior occurs, its stored energy per unit volume of grain boundary area decreases. Comparing the KAM maps of the low and high temperature HAZ regions, refer to Fig. 7 b) and Fig. 8 b), respectively, reveals a significant increase in the fraction of KAM values between 0 and 0.4 ° for the high temperature HAZ (74.6–82.7%), with a decrease in the 0.4 to 0.8° range (22.3–16.4%). This change evidence the effect of high temperature in the promotion of a reduced dislocation density of the previously highly deformed BM. Moreover, owing to the dependence of the consumption of stored energy with temperature, it is also clear that high temperatures and/or permanence times are conducive to a more significant reduction in the material stored energy.

Despite the higher temperature experienced by the HAZ near the FZ region, there was not change in the phase content, with the microstructure being dominated by the FCC phase (≈97.5%) with trace amounts of BCC Cr–Mn-based oxides (≈2.5%), as shown in Fig. 8 c).

The fraction of $\sum 3$ twin boundaries decreased to ≈29.8% in the HAZ near the FZ region (refer to Fig. 7 d) and Fig. 8 d)). This is again attributed to the high temperature experienced by this region of the welded joint. In fact, the reduction in the fraction of $\sum 3$ boundaries is related to the grain growth process, where grains collide with each other, causing a reduction in the mobility of the grain boundaries. Besides, the rapid movement of adjacent grain boundaries or twins can easily consume preexisting twin boundaries during grain growth, resulting in the partial or full annihilation of the previously existing annealing twin boundaries, which ultimately leads to a reduction in the number of annealing twins as grain growth proceeds. Finally, when the grain growth process is finished, large grains will exist, while stable twins can be kept in the material microstructure. This assessment has been previously confirmed in [43,44], where it was shown that annealing twins can gradually disappear through migration of grain boundaries or twin boundaries during grain growth. It should be noted that, in this work, annealing twins were only observed in the HAZ of the welded joint.

Fig. 9 details the EBSD data obtained at the HAZ/FZ interface which can be used to elucidate on the epitaxial growth phenomenon experienced in the FZ. When entering the FZ, small equiaxed and columnar grains nucleate from the cold substrate. Here, the temperature gradient is maximum, which enables to obtain a refined grain structure compared to the bulk of the FZ. Moreover, at the fusion zone boundary, there is no evidence of preferred orientation (refer to Fig. 9 a). While progressing away from the HAZ/FZ interface toward the weld centerline, there is a decrease on both the temperature gradient and cooling rate, and the tendency for a refined grain structure to be formed significantly decreases. In fact, columnar-like grains start to be predominant roughly 30 μm away from the FZ boundary. These coarse columnar grains will grow in the opposite direction to the heat flow extraction and nearly perpendicular to the FZ boundary. Grains that have their preferential growth direction aligned with the heat flow extraction will have their growth facilitated.

Quantification of the average KAM values shown in Fig. 9 b) revealed that the peak of residual strain occurs on the boundary line of HAZ/FZ interface within the refined grain structure that exists at this location. This can be attributed to thermally induced strains derived from the large heat input of arc-based processes. In the presence of the cold substrate, the cooling rate is significantly more abrupt preventing the material to freely accommodate these thermal strains upon cooling and subsequent solidification. Towards the bulk of the FZ, the thermal
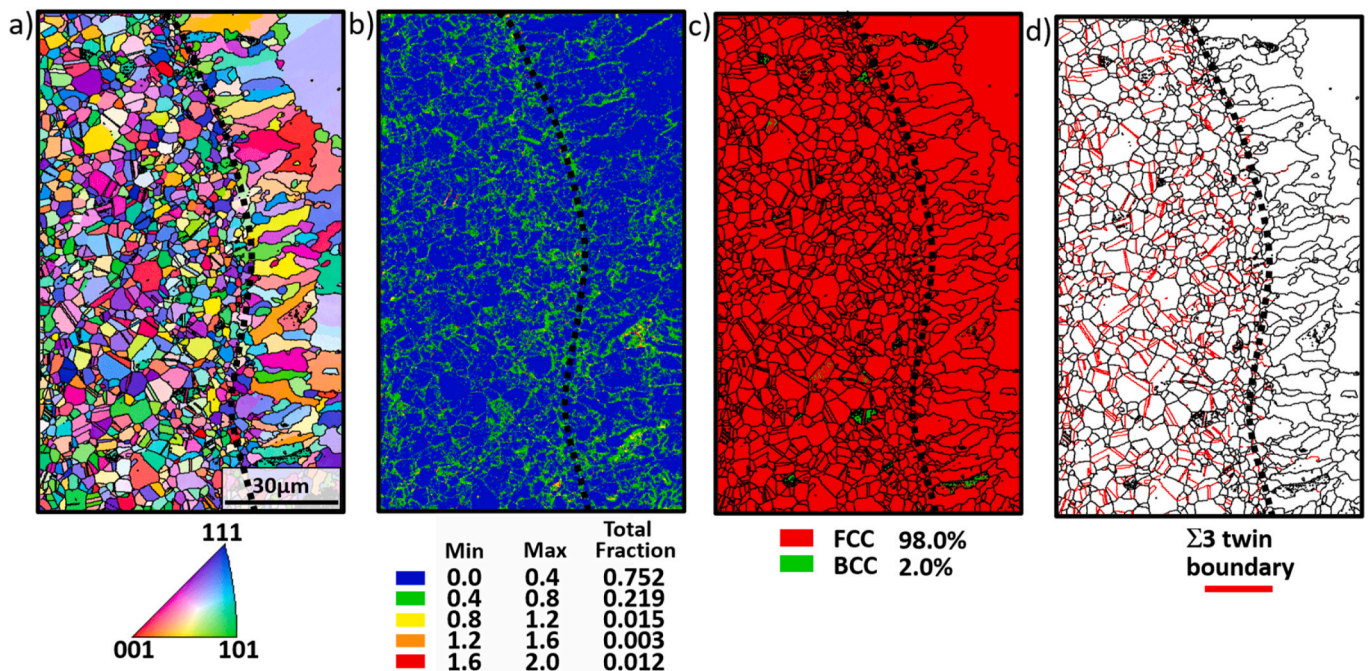

Fig. 9. EBSD analysis of the HAZ/FZ interface: a) IPF map; b) KAM map; c) phase diagram map; d)$\sum 3$ twin boundaries map.

conditions are not as severe, since the thermal gradient is reduced, which allows the material to more easily accommodate the thermal strains. Nonetheless, it should be mentioned that the KAM values obtained at this location are, in magnitude, lower than those in the BM, implying that despite the occurrence of thermal strains due to the weld thermal cycle, these are not as severe as those imposed by the cold rolling of the BM.

The EBSD phase map shown in Fig. 9 c) details that the phase constituents near the HAZ/FZ interface are again the FCC phase (97.5%) and the BCC phase (2.5%). Thus, even though the peak temperatures are maximum at this location, while staying below the CoCrFeMnNi BM melting point, there was no significant influence on the existing phases and their volumetric fraction.

Interestingly, the $\sum 3$ annealing twins observed in the HAZ region (refer to Fig. 7 d) and Fig. 8 d)) disappear when crossing the HAZ/FZ interface towards the FZ (refer to Fig. 9 d)). This is related to the fact that upon melting any previous thermomechanical processing is lost. Thus, the effect of rolling followed by permanence times at relatively high temperatures is not preserved, with the resulting material microstructure resembling that of the material in the as-cast state.

Within the center of the FZ, the previously fine equiaxed and columnar grains transform into coarse columnar grains that preferentially grew perpendicular to the fusion boundary (refer to Fig. 5). Most grains at the edge of the FZ are oriented along the <0 0 1> and <1 0 1> preferred growth orientations, suggesting that grain growth in the <1 1 1> orientation is inhibited, this being attributed to the competitive grain growth mechanism occurring during solidification [45]. The evolution of the microstructure within the FZ is in line with the solidification theory of fusion welding [46], i.e., the larger cooling rate at the boundary of HAZ and FZ, which is determined by the thermal gradient and growth rate product, promoted the formation of a small grain structure, which eventually turned into coarse columnar grains when the temperature gradient was reduced towards the weld centerline.

Although the FZ is again predominantly composed of FCC phase ($\approx$96.0%), a small amount of the previously reported BCC phase was also detected, as detailed in Fig. 9 c). Although not detected by EBSD owing to the small volume fraction, it should be mentioned that σ phase was detected upon the use of synchrotron X-ray diffraction. The formation of σ phase within the FZ will be described together with the synchrotron X-ray diffraction data detailed in Fig. 12 d).

No evidence of twins was observed in the bulk of the FZ (as depicted in Figs. 5 and 9 d)), due to the remelting and fast solidification experienced by the material, which would promote the development of a microstructure similar to that of casting processes [47]. Besides, it is worth mentioning that in the FZ, there is no driving force for annealing twins to be formed, since the thermal stresses resulting from the welding procedure are not conducive to the formation of these features.

Fig. 10 a) to e) detail a large-scale EDS map performed across the FZ of the joint for the main elements (Co, Cr, Fe, Mn and Ni) that compose it. Fig. 10 f) details the analyzed area, while the white dashed lines delimitate the HAZ/FZ interface, and the black dashed line corresponds to the local of the EDS line scan detailed in Fig. 10 g). During fusion-based welding, elemental redistribution is a typical feature within the FZ. The molten pool behavior is dominated by complex patterns that derive from the Marangoni currents which depend, among other things, on the local temperature, composition and density. Moreover, the poor mixing between the base and filler materials can also lead to the formation of complex patterns across the FZ.

Overall, the EDS mapping results show a good mixture of different elements that compose both the CoCrFeMnNi BM and the ER-410 filler material, with a relatively uniform distribution of elements and no evidence of macrosegregation. The EDS line scan detailed in Fig. 10 g), shows a significant Fe enrichment within the FZ compared to the BM. This was already expected owing to the fact that the ER-410 filler material is Fe-rich. The amount of Cr within the FZ is kept approximately the same compared to the BM, while the remaining elements evidence a decrease upon the dissolution of the filler material within the melt pool. The high temperatures experienced by the melt pool during welding can also aid in the preferential loss of certain elements. In particular, Mn loss can be favored due to its low melting and boiling points, as well as higher vapor pressure.

As detailed when presenting the EBSD data, across the joint it was identified the presence of a secondary phase. To promote its identification EDS analysis was also performed. The morphology and composition maps obtained in representative regions of the BM, HAZ and FZ are detailed in Fig. 11 a), b) and c), respectively. This data confirms the presence of Cr–Mn-rich oxides. In fact, the detection of such Cr–Mn-rich oxide particles in the CoCrFeMnNi high entropy alloy is common [30, 48], which is mainly attributed to the potential contamination of the raw material, as well as oxidation occurring during the casting procedure. Although both the top and bottom surfaces of the welded specimens were protected during the welding process using argon, this still did not avoid the formation of this phase in the FZ zone. This is common in arc-based processes, and is related to the high heat source dimensions and potential turbulent flow of the gas during the process. Previously, Kim et al. [49] investigated the high temperature oxidation behavior (between 900 and 1100 °C) of the CoCrFeMnNi high entropy alloy, and found that at high temperatures, Cr–Mn-based oxides are easily formed owing to the high affinity of these two elements with oxygen at those temperatures. The presence of such oxide particles detected in the FZ
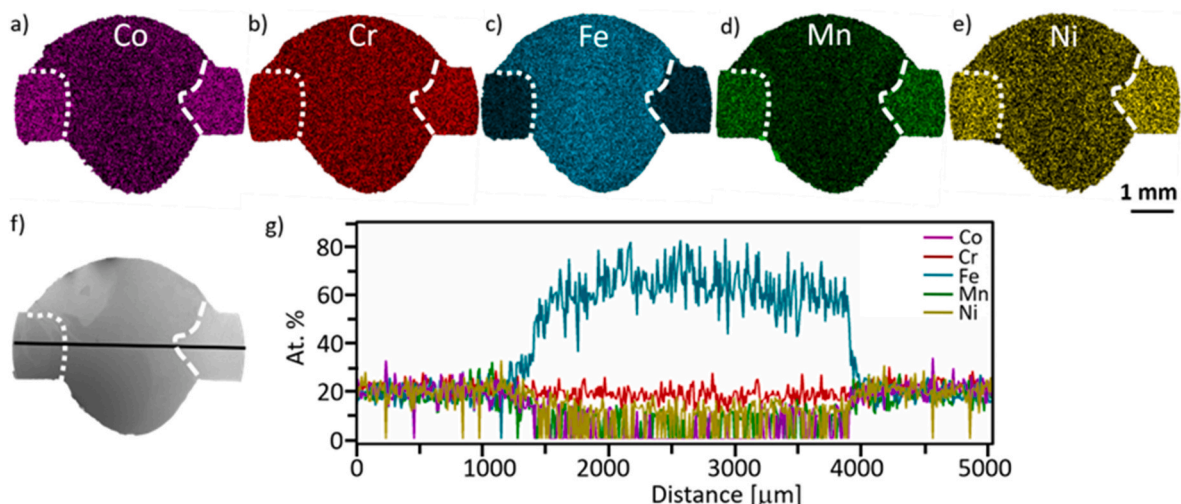

Fig. 10. a) – e) EDS mapping of the welded joint; g) EDS line scanning across the weld along the black line of f).
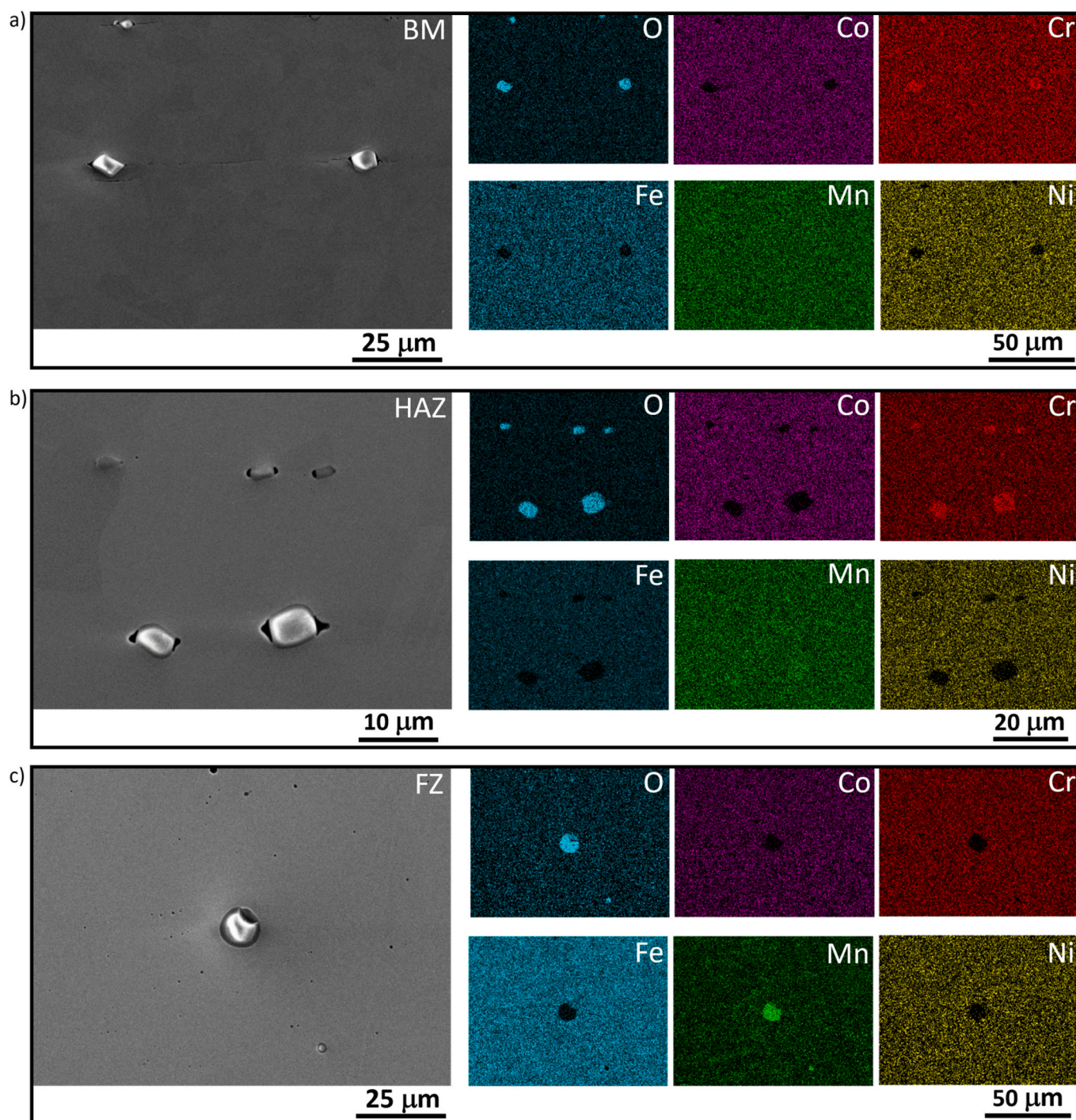
Fig. 11. SEM images and corresponding EDS mapping of Cr–Mn-based oxides: a) BM; b) HAZ; c) FZ.

prove that at high temperatures, and even with the use of inert shielding gas, it is difficult to avoid the formation of such oxides in this high entropy alloy system. It should be mentioned that the presence of these oxide particles are not always detrimental to the mechanical properties of the material, as their volume fraction will play a role on the resulting mechanical performance [50].

3.2. High energy synchrotron X-ray diffraction

Fig. 12 a) depicts the superimposition of the X-ray diffraction patterns obtained at room temperature across the welded joint. To better understand the microstructural changes between the different regions,

typical representative diffraction patterns for each region (BM, HAZ and FZ) are detailed in Fig. 12 b) – d). The phase volume fractions, as obtained by Rietveld refinement, are depicted in Table 3. The effects of the weld thermal cycle on the existing phases and their volume fraction over the welded joint are explored next in combination with the previous electron microscopy characterization data.

Overall, Fig. 12 a) reveals minor microstructure variation among the BM and the HAZ regions, with evident changes occurring in the FZ. Considering the representative individual diffraction patterns depicted in Fig. 12 b) - d) it is possible to observe the presence of Cr–Mn oxides in all three regions. Although the phase volume fraction of these Cr–Mn oxide particles increases slightly when determined using the diffraction
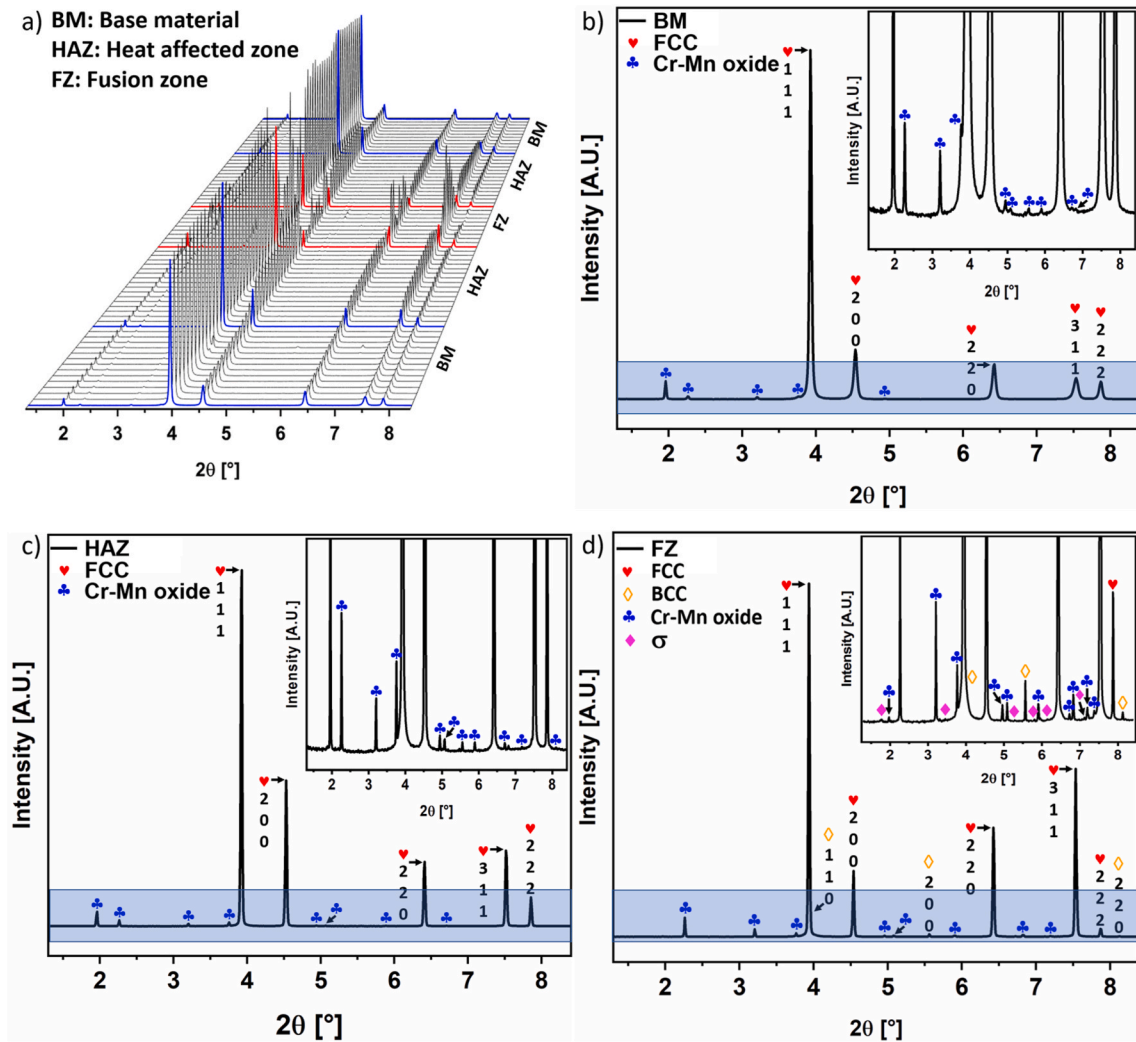
Fig. 12. 3D plot and phase identification of existing phases within the welded joint using high energy synchrotron X-ray diffraction: a) superimposition of diffraction patterns across the welded joint; b), c) and d) are representative diffraction patterns from the BM, HAZ and FZ, respectively. The blue boxes highlight the inserts of a), b) and c) diffraction patterns. (For interpretation of the references to color in this figure legend, the reader is referred to the Web version of this article.)

Table 3
Volume fraction evolution of the FCC, Cr–Mn oxide, BCC and σ phases across the welded joint as obtained by Rietveld refinement.

Phase volume fraction [%]					
		Disordered FCC	Cr–Mn oxide	Disordered BCC	σ
Region	BM	~98.7%	~1.3%	–	–
	HAZ	~98.2%	~1.8%	–	–
	FZ	~94.5%	~2.5%	~2.3%	~0.7%

data (1.3, 1.8 and 2.5% in the BM, HAZ and FZ, respectively), it is expected that these volume fractions do not have a detrimental effect on the mechanical performance of the welded joint [50]. Besides, the slightly higher volume fraction of these oxides in the FZ can be related to (minor) oxygen pick up during welding.

Besides the Cr–Mn oxide particles, only a disordered FCC phase was identified in the BM and HAZ regions, which is the typical microstructure of this material when it undergoes rolling or short to medium time heat treatments [51]. Interestingly, more phases formed in the FZ upon the addition and mixing of the ERNiMo-410 filler wire. In addition to the FCC matrix phase (≈96.3%) and the Cr–Mn oxides, it was identified the presence of another BCC phase (≈2.3%), as well as of σ phase (≈0.7%). The appearance of these two phases (BCC and σ) is the result of

compositional differences caused by the dilution of the ER410-NiMo stainless steel filler wire with the BM, which translates into a different solidification behavior. Previous work by Qin et al. [52] have studied the effect of the addition of Mo on the microstructure evolution of CoCrFeMnNi high entropy alloys, and showed that the addition of this element can facilitate the formation of Mo-rich σ phase. However, the current work did not observe any evidence of Mo-rich precipitates. This absence of Mo-rich precipitates is likely due to the small fraction of Mo that exists in the filler material, which is then further diluted into the melt pool during welding, thus not being conducive to the formation this Mo-rich phase. Moreover, the addition of Cr, which exists in FZ coming from both the BM and filler wire, can aid in the formation of σ phase. Previous work by Zaddach et al. [53,54], have shown that when the Cr to Ni ratio increases, as it occurs in the bulk of the FZ zone, the formation of σ phase is enabled by the reduction of the material stacking fault energy. It is worth mentioning that the σ phase is not detected by EBSD due to its small volume fraction (≈0.7%), showcasing the potential for high energy synchrotron X-ray diffraction to fine probe complex microstructures even for phases with residual volume fractions. More details on the composition of the existing σ phase will be presented alongside with the thermodynamic calculations. Moreover, the effect of the dilution rate of the ER410-NiMo martensitic stainless steel filler wire on the microstructure of the FZ will be discussed in the next sections.

Since the full width at half height (FWHM) of X-ray diffraction peaks is typically sensitive to both microstrain and grain size effects, the analysis of the FWHM of selected diffraction peaks along the welded joint can help to trace the effects of the weld thermal cycle on micro-structural evolution [55]. Here, focus is given to the (2 2 0) and (3 1 1) diffraction peaks. The former was selected due to its relatively high in-tensity and lack of neighboring peaks that could interfere with the single peak fitting routine, while the latter was selected due to its insensitivity to intergranular stresses [56]. Moreover, taking advantage of the 2D diffraction images obtained during the synchrotron radiation diffraction measurements, it is possible to analyze the orientation dependence of certain microstructure features within the laboratorial reference frame. Thus, the raw data was integrated along the 0 and 90 ° azimuthal angles, which correspond to the parallel and perpendicular directions of the welded joint, respectively, as previously indicated in Fig. 3.

Fig. 13 details the variation of the FWHM along both directions and it can be observed that both have the same pattern, although the magni-tude of the observed changes is distinct. The largest FWHM values are observed in the BM region, which confirms that the BM possesses high plastic strain arising from the rolling process. Moreover, it can be inferred that this region of the base material has a high dislocation density, since heavily deformed regions tend to show a relatively broader diffraction profiles [57]. When entering in the HAZ, a signifi-cant reduction in FWHM is observed. Here, it is important to mention that the main factors contributing to a reduction of FWHM are coarse grain sizes, as well as decreased microstrain and dislocation density. Evidently, in the HAZ, recovery, recrystallization and grain growth reduce the dislocation density and release the strain energy stored in the BM, which is predicted to induce a softening behavior at this location, except if strengthening phases are formed due to the weld thermal cycle. Interestingly, in the FZ, no diffraction peaks are observed in some re-gions, which is related to the large and highly oriented columnar grains which do not diffract for certain azimuthal orientations. This is referred to as a textural effect, which is a typical feature of the non-equilibrium solidification conditions experienced by FZ [33].

As it will be discussed later, the evolutionary trend of the FWHM and the hardness distribution (presented in Figs. 13 and 17) have almost the same profile. However, closer inspection reveals that the HAZ extension,
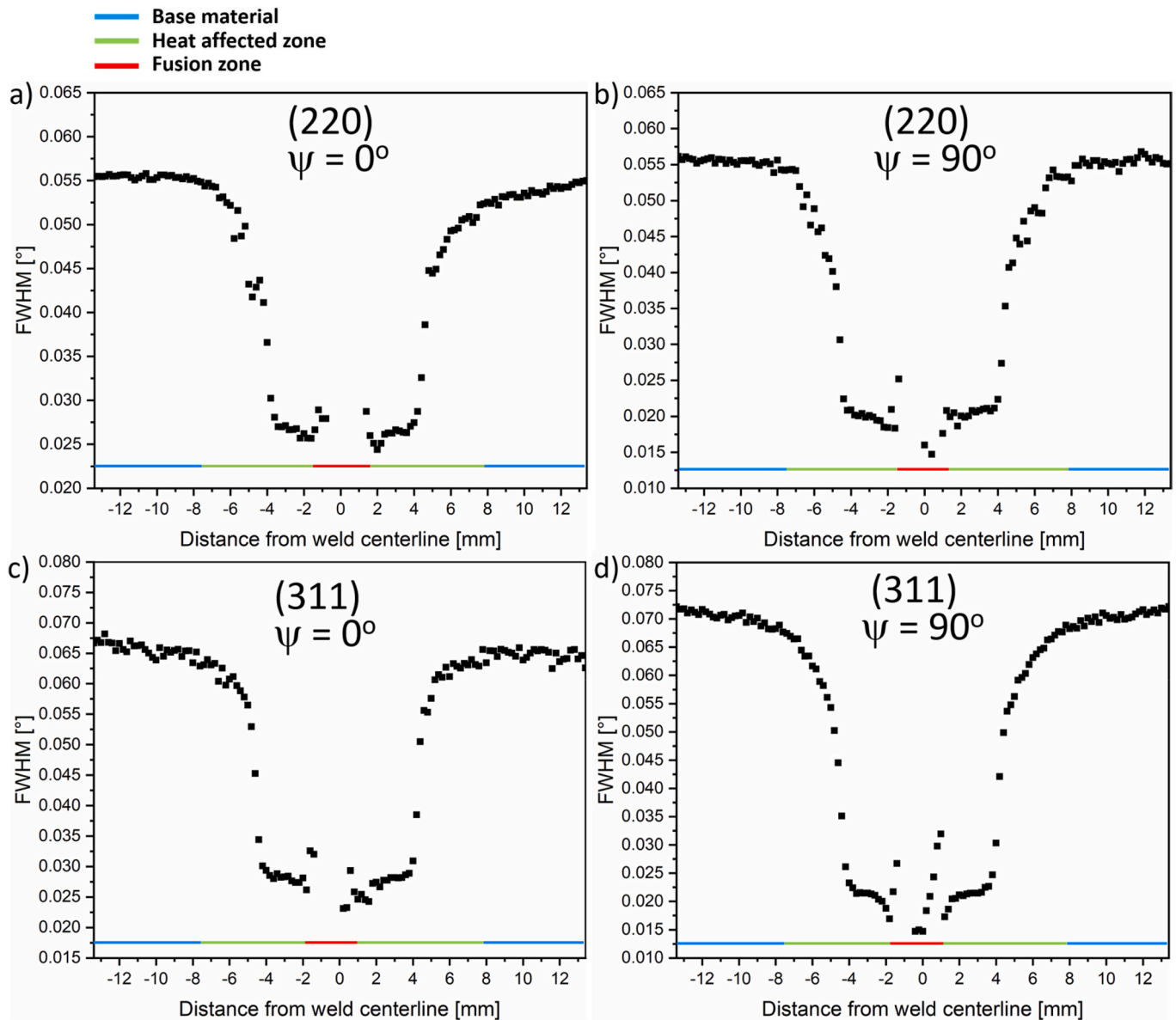

Fig. 13. Evolution of the FWHM for the CoCrFeMnNi gas metal arc welded joints considering the (2 0 0) and (3 1 1) diffraction peaks integrated along the 0 and 90° azimuthal angles.

as captured through the FWHM analysis, is slightly larger than that captured using microhardness mapping. This is related to the effect of the weld thermal cycle, which, in the low temperature HAZ, promotes the occurrence of recovery thus translating into less structural defects in the material, although without any appreciable change in the material microhardness [33]. Based on this, and combining the distribution of hardness (Fig. 17) and the evolution of the FWHM (Fig. 12), the width of the heat affected zone is of ≈ 6 mm (half on each side of the joint). Within the heat affected zone, the regions where recovery, recrystallization and significant grain growth occur have an extension of ≈1, ≈3.5 and ≈ 1.5 mm, respectively.

3.3. Thermodynamic calculations

To predict the effect of different dilution ratios (mixing ratio between the BM and filler material) on the solidification path experienced by the fusion zone, thermodynamic calculations were performed based on the Scheil-Gulliver model considering 10% dilution steps. Here, 0% dilution represents the FZ containing only ER410-NiMo stainless steel filler wire, while 100% dilution corresponds to the FZ consisting only of the CoCrFeMnNi high entropy alloy. As detailed in the experimental procedure, the role of C as a fast diffuser was also evaluated.

The potential solidification paths considering C as a fast diffuser are detailed in Fig. 14 and it is clear that the solidification path is closely related to the dilution ratio of the ER410-NiMo filler wire. Nonetheless, regardless of the dilution considered, the FCC phase is always present. When the dilution ranges between 0 and 40%, i.e., when the ER410-NiMo stainless steel filler wire is predominant in the FZ, the phase structure formed by rapid solidification will include a BCC phase. When the dilution ratio varies between 40 and 60%, σ phase formation is favored. Above these ratios, σ phase formation is inhibited.

Fig. 15 was obtained to evaluate and compare the accuracy of the Scheil-Gulliver calculations when C was not selected as a fast diffuser. The same dilution steps (10%) and chemical composition were used, with the only difference being that no element was selected as a fast diffuser.

As can be seen from Fig. 15, the solidification path still varies with the variation of the dilution ratio. However, comparing with Fig. 14, it can be noticed that the phases formed with and without C being selected as fast diffuser are different under the same dilution ratio. For example, for a 10% dilution ratio, when C is selected as fast diffuser, the solidification path is Liquid → Liquid + BCC → Liquid + BCC + FCC (refer to
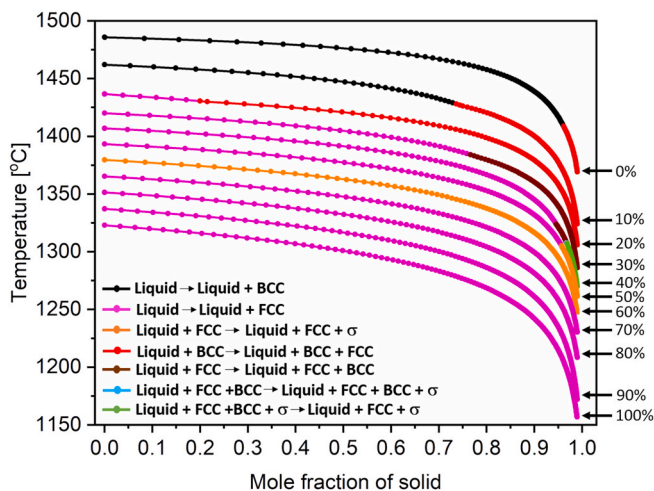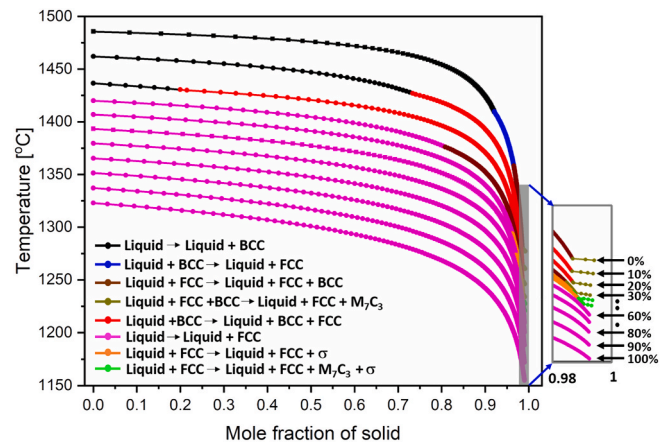

Fig. 15. Scheil-Gulliver calculations for the CoCrFeMnNi high entropy alloy with ERNiMo-410 filler wire welded joint considering different dilution conditions without C as a fast diffuser. 0% dilution rate corresponds to the ERNiMo-410 martensitic stainless steel, while 100% dilution corresponds to the CoCrFeMnNi high entropy alloy. The grey box details a close-up view of the solidification paths for mole fraction values above 0.98.

Fig. 14), but when C is not considered as a fast diffuser, the solidification path obtained is Liquid → Liquid + BCC → Liquid + BCC + FCC → Liquid + FCC + M_7C_3.

Evidently, the dilution ratio of ERNiMo-410 filler wire and the diffusion rate of C are both influential factors for the phase formation in the FZ. Nevertheless, when both conditions varied, the first phase to form (and that is kept during solidification) is the FCC. The BCC phase only appears for a dilution range between 0 and 40%, suggesting that the BCC phase was also independent of the C diffusion rate (refer to Figs. 14 and 15). Removing C as a fast diffuser, only enables the formation of the σ phase for 40–50% dilution ratios, while only a single FCC phase is formed when the dilution ratio is above 50%, which is slightly different from the results predicted when C was set as fast diffuser. The most significant difference is the predicted formation of M_7C_3 carbides for a wide dilution ratio range (0–50%) when C was not selected a fast diffuser. When this element was imposed a fast diffuser no carbides where thermodynamically predicted. It is worth mention here that thermodynamic calculations predict that the σ phase that is formed in the FZ will be Fe–Cr- or Cr–Mn-rich. EDS mapping near one particle of this phase, detailed in Fig. 16, shows an enrichment in both Cr and Mn, which further validates these thermodynamic calculations.

Importantly, coupling of the synchrotron X-ray diffraction data (shown in Fig. 12 d)) enables to confirm that the most likely solidification path is that obtained when considering C as a fast diffuser. In fact, no evidence of M_7C_3 across the FZ was observed. Thus, the predicted phases using the Scheil-Gulliver model with C set as a fast diffuser are in good agreement with the high resolution diffraction data obtained.

3.4. Mechanical behavior

Microhardness mapping was performed on the welded joints to further investigate the relationship between the microstructure and local strength across the welded material. Fig. 17 a) details the 2D microhardness map of the whole welded joint, identifying the three regions of the joint (BM, HAZ and FZ). The results show that the hardness values of the BM, HAZ and the FZ differ significantly, with a U-shaped distribution trend.

The BM has the highest hardness of about ≈400 HV0.5, which is due to the strain hardening imposed by cold rolling. Here, it is worth mentioning that the hardness of the base material used in this work is slightly higher than that reported in [29], which is related to the location from where the base material sheets were removed after rolling
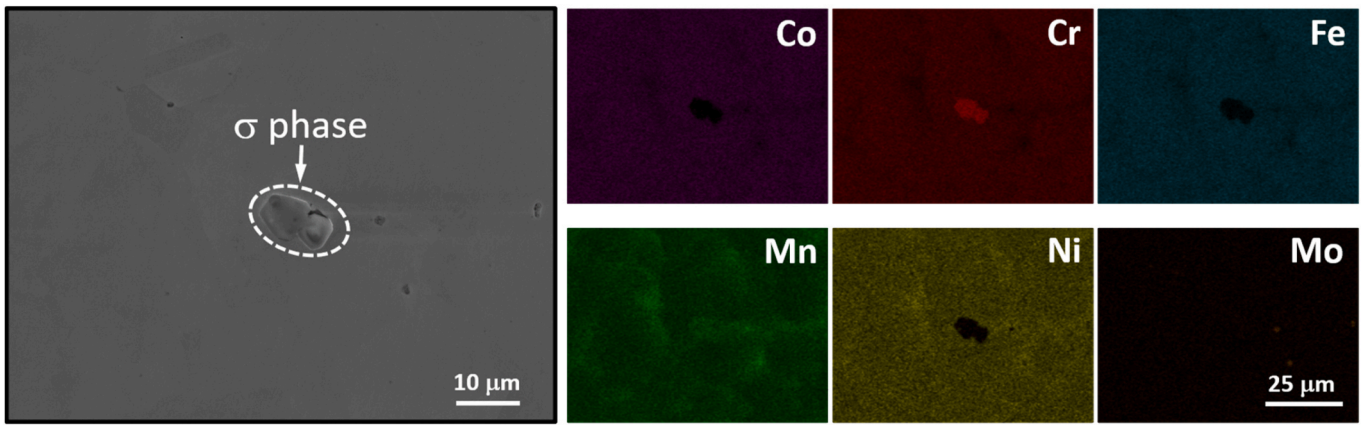

Fig. 14. Scheil-Gulliver calculations for the CoCrFeMnNi high entropy alloy with ER410-NiMo filler wire welded joint considering different dilution conditions using C as a fast diffuser. 0% dilution rate corresponds to the ER410-NiMo martensitic stainless steel, while 100% dilution corresponds to the CoCrFeMnNi high entropy alloy.

Fig. 16. SEM images and corresponding EDS mapping near one particle of σ phase.
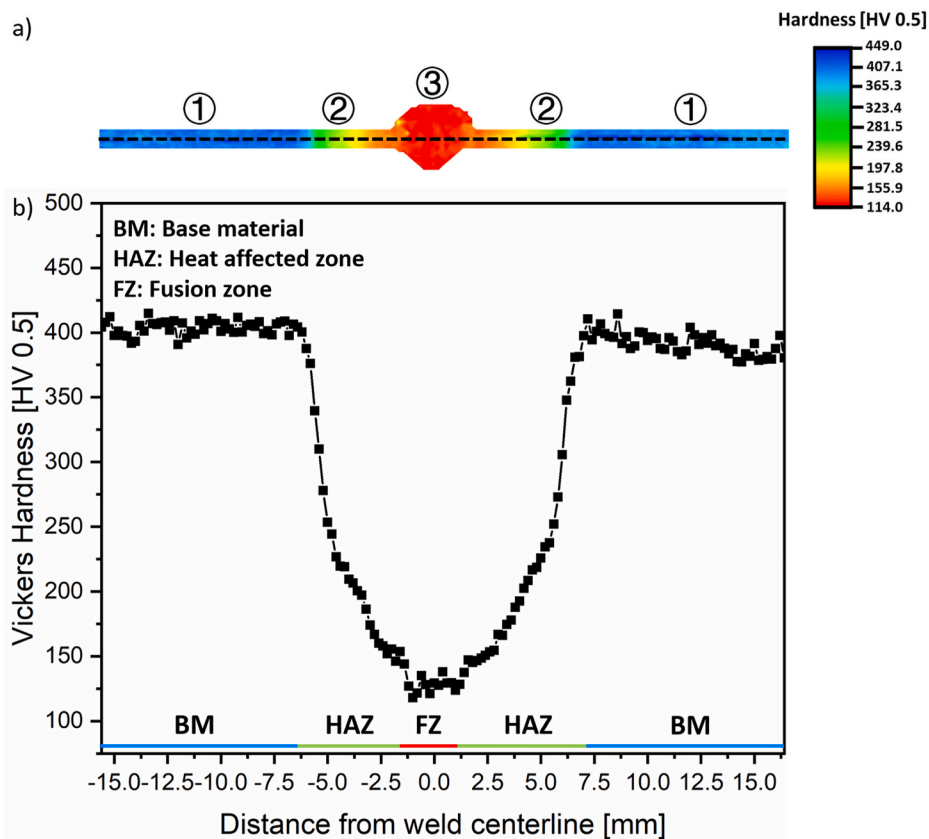

Fig. 17. a) Microhardness map across the welded joint; b) microhardness profiles obtained at the middle of the joint (black dashed line across the hardness map of a)).

[58]. When entering the HAZ, the material starts to exhibit a softening behavior, and the hardness decays from ≈400 to ≈150 HV0.5. This reduction in hardness is attributed to the thermal cycle experienced by the HAZ, which promotes an annealing-like heat treatment promoting both grain recrystallization and growth. However, the extent of these two solid state transformations differs depending on distance to the heat source. Thus, closer to the BM, the prevalence of recrystallization with associated minor grain growth leads to a reduced decrease in the material hardness, within the 250 to 350 HV0.5 range, whereas closer to the FZ grain growth overturns recrystallization as the main solid state transformation leading to an abrupt decrease in hardness down to 150 HV0.5. However, unexpectedly, the lowest hardness across the joint (≈125 HV0.5) occurs in the FZ. The average hardness across the FZ is similar to that of as-cast CoCrFeMnNi high entropy alloys [59]. This suggests that the different composition induced by the mixing of the filler material within the FZ is not conducive to an evident solid strengthening. It should be stated that the large grain size of the fusion zone also aids in the development of low hardness at this location, as known from the Hall-Petch effect. In addition, small fluctuations in microhardness were observed in the FZ, which may be related to complex composition changes induced by the chaotic fluid flow typical of fusion-based welding processes. Based on the above analysis, it can be concluded that the variation in the hardness distribution in the welded joints is closely related to the homogeneity of the microstructure, degree of recrystallization and grain size evolution, as well as dislocation density.

To evaluate the effect of the addition of the ER410-NiMo filler wire on the joint mechanical properties, the stress-strain curves of the gas metal arc welded joints obtained with the ER410-NiMo filler wire were benchmarked against gas tungsten arc welded joints obtained without addition of filler wire (with the latter welds being done by the present research team as detailed in [33]), as depicted in Fig. 18. The solid and dashed lines represent the engineering and true strain-stress curves, respectively. A summary of the mechanical properties (yield strength, ultimate tensile strength and ductility) is shown in Table 4. Comparing the tensile mechanical behavior of the two welded joints, it can be seen that the welded joint with the addition of filler wire is clearly superior to the gas tungsten arc welded joint in terms of both yield strength (355 vs 284 MPa) and ultimate tensile strength (641 vs 519 MPa). This is mainly attributed to the excess weld metal introduced by the added filler wire (refer to Fig. 4) [60], which increases the cross-sectional area of the FZ, resulting in a location where the stress per unit area under the same tensile external load is significantly lower than that imparted in the BM and HAZ. Thus, the presence of weld face/root reinforcement promotes an overall increase in both the yield and tensile strength of the gas metal arc welded welded joint compared to the filler-free welded material. Although, the face and root reinforcements can aid in increasing the stress imparted by the material, it can also promote stress concentrations, especially at the weld toe. This can make crack initiation and propagation at those locations easier thus accelerating joint fracture. This can be the reason for the reduced ductility of the joint. Nonetheless, the gas metal arc welded joint still exhibits a ductile behavior with potential to be considered for structural applications.

Fig. 19 a), b), c) and d) detail digital image correlation snapshots taken at different stages of deformation, namely during elastic deformation, macroscopic yielding, uniform plastic deformation and right before fracture, respectively, showing the strain distribution along the joint. During the elastic deformation stage (refer to Fig. 19 a)), the deformation is uniform over the welded joint and the maximum local strain is small. When macroscopic material yielding occurs (refer to Fig. 19 b)), there is a significant increase in the maximum strain, ($\varepsilon \approx 1.1\%$), but the differentiation between the BM, HAZ and FZ is not obvious. When entering the uniform plastic deformation regime (refer to Fig. 19 c)), significant stress concentration at the HAZ/FZ interface is observed, where a maximum local strain of 5% is reached. Prior to fracture of the material (refer to Fig. 19 d)), the BM, HAZ and FZ regions of the welded joint can be clearly distinguished, as the strain concentration at the HAZ/FZ interface is now significant. By combining this
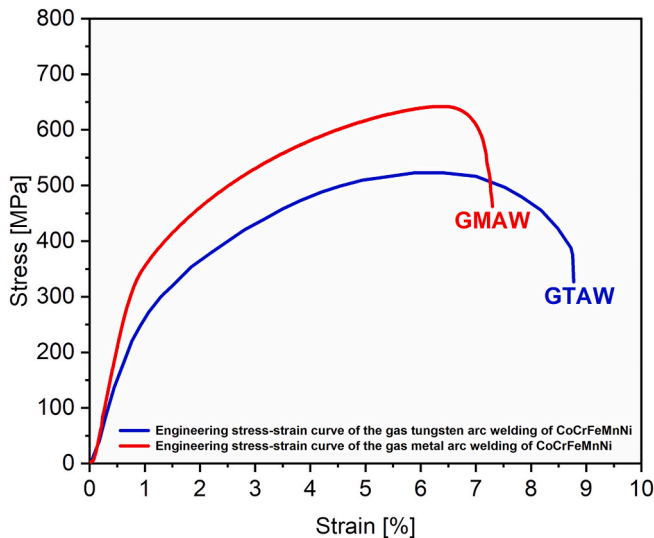
Table 4
Summary of tensile properties of BM, gas tungsten arc welded CoCrFeMnNi (obtained from [33]) and gas metal arc welded CoCrFeMnNi with ER410-NiMo filler material.

Sample	Yield strength [MPa]	Ultimate tensile strength [MPa]	Ductility [%]
Base material (from [33])	587 ± 7	943 ± 6	9.5 ± 0.2
Gas tungsten arc welded joint with no filler wire (from [33])	284 ± 4	519 ± 3	8.4 ± 0.4
Gas metal arc welded joint with ER410-NiMo filler wire	355 ± 10	641 ± 7	7.3 + 0.2

mechanical response information with the previous microstructure characterization, it can be inferred that the stress concentration observed in the strain map prior to failure is due to the joint reinforcement (refer to Fig. 4 a)). Failure initiated at the weld toe propagating along the HAZ/FZ interface. The main reason for fracture occurring at this location is related to a stress concentration effect caused by the excess of material in the FZ. Although not discussed due to lack of available material, it is possible to further tune the welding process parameters to obtain smoother reinforcement profiles, which can then help to alleviate the stress concentration issues and aid in obtaining improved mechanical properties of the joint, especially in what concerns its ductility.

To gain a more detailed understanding of the mechanical behavior of the different regions over the welded joint during tensile testing, the raw digital image correlation data was further processed to determine the stress-strain curves of the BM, HAZ, weld toe (fracture initiation location) and FZ. These results are shown in Fig. 20, where the black, pink, red and blue lines represent the local tensile stress-strain curves for each of these four regions.

Each region shows different mechanical behavior, which is mainly caused by two factors. The first is due to changes in microstructure caused by the weld thermal cycle. The second is attributed to shape-related defects due to the face/root reinforcement in the FZ which favors the occurrence of preferential stress concentrations.

Based on the mechanical response of each region during macroscopic elastic deformation, the Young's modulus was determined to follow $E_{FZ} < E_{HAZ} < E_{BM}$. The variation of the Young's modulus is in good agreement with the microstructure and hardness characterizations previously performed: the highly deformed BM has the highest modulus and hardness, while the opposite occurs for the FZ. The HAZ mechanical properties lie between these two regions.

Considering the total deformation imparted by each region, it is observed that the BM only deformed by $\approx 1.8\%$ before joint failure occurred. This is related to the strain hardening experienced by the material prior to welding. Hence, the onset for plastic deformation to occur is delayed compared to the remaining softer regions of the joint. This means that there is a load partitioning effect, where the low hardness regions will be preferentially deformed during loading of the welded joint. Interestingly, despite being the softer region, the strain in the FZ is only around 4.8%. This significantly contrasts with the strains measured in the HAZ region (up to 16.8%) and near the weld toe (32.0%) where failure occurred. This is an apparent contradiction when considering the local hardness and the likely stress distribution during mechanical loading. In fact, this is related to the addition of the ER410-NiMo filler metal which increases the effective cross-sectional area in the FZ (refer to Fig. 4 a)) by comparison with welding processes without addition of filler material. Looking at the cross-sectional area of the FZ, it is observed that this region is almost three times larger than in the remaining joint, leading to a smaller force per unit area imparted by the FZ under the same external tensile loading. Consequently, the plastic deformation over the whole FZ region will be reduced, causing the
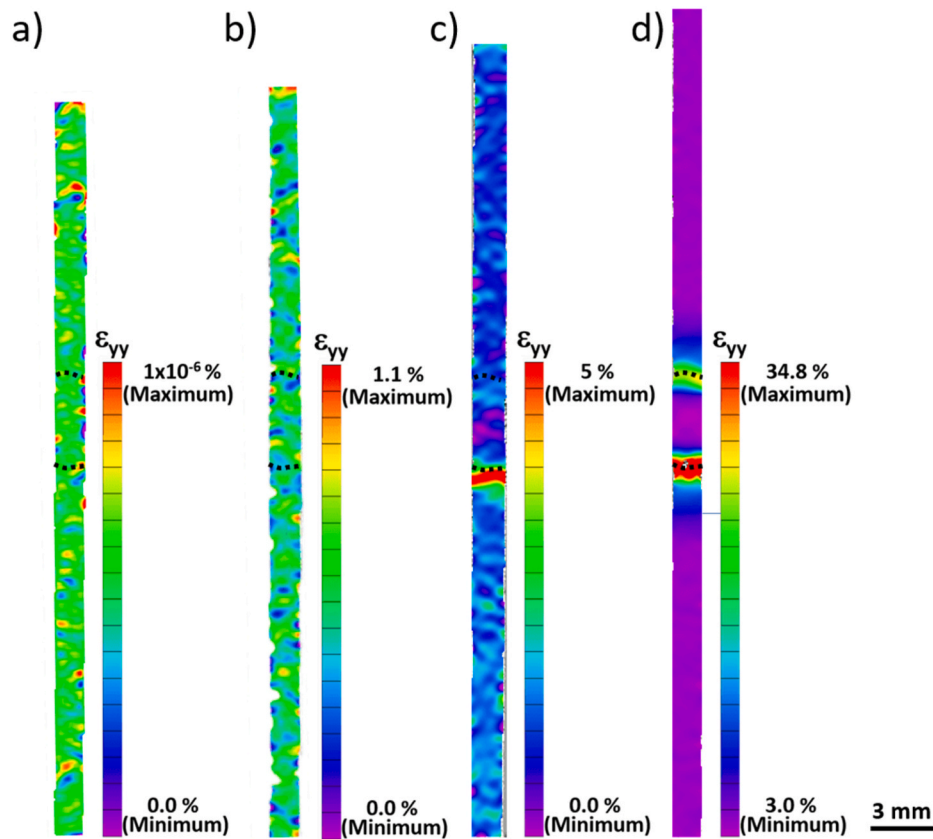

Fig. 18. Representative engineering stress-strain curves of a gas tungsten arc welded CoCrFeMnNi (obtained from [33]) and gas metal arc welded CoCrFeMnNi with ER410-NiMo filler material.

Fig. 19. Digital image correlation snapshots obtained at different loading steps during: a) macroscopic elastic deformation; b) macroscopic yielding; c) uniform plastic deformation; and d) before joint fracture.
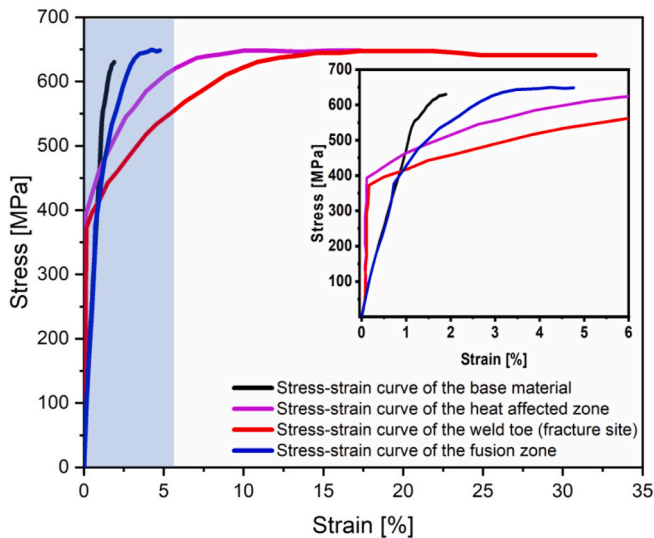

Fig. 20. Tensile curves obtained from the digital image correlation measurements for different regions across the joint: BM (black line), HAZ (pink line), weld toe (red line) and FZ (blue line). The light blue region is zoomed in the insert. (For interpretation of the references to color in this figure legend, the reader is referred to the Web version of this article.)

amount of deformation in the softer FZ region to be lower than that in the HAZ region and near the weld toe site. However, the amount of deformation in the FZ region is still slightly higher than that of the BM (4.7 vs 1.8%), which suggests that the significantly higher hardness in the BM (400 vs 125 HV0.5) prevails in resisting to plastic deformation.

Conversely, the amount of deformation at the weld toe site reaches its maximum at fracture, approximately 32.0%, as a result of the stress concentration acting on the smaller cross section area and relatively softer region (compared to the BM).

Based on the stress-strain curves of the different regions of the joint shown in Fig. 20, the load transfer behavior can also be predicted. Specifically, at the onset of deformation, the FZ is the softest region and takes on more load. When it starts to yield, the FZ and the weld toe site also consecutively yield, while the BM region is still only being elastically deformed due to the previous strain hardening. Theoretically, with further deformation, the load should be transferred to the BM, owing to the strain hardening occurring at the remaining regions. However, due to the presence of face and root reinforcement in the welded joint, stress concentration points are easily enabled thus promoting the preferential local deformation at the weld toe as shown in Fig. 19. Therefore, after the FZ, HAZ and weld toe have yielded, there is not a significant load transfer to the BM region.

Fig. 21 details a SEM image of the fracture surface of the welded joint. It is well know that dimples are the primary feature associated to ductile fracture in polycrystalline metals [61]. Here, a large number of dimples with various diameters were observed, which agrees well with the good plasticity of the welded joint, as detailed by the tensile and digital image correlation data. Minor particles are observed sparsely distributed. These particles correspond to the previously identified Cr–Mn-based oxides [24].

4. Conclusions

In this work, gas metal arc welding of CoCrFeMnNi high entropy alloy using ER410-NiMo stainless steel filler wire was performed. By combining advanced material characterization, thermodynamic
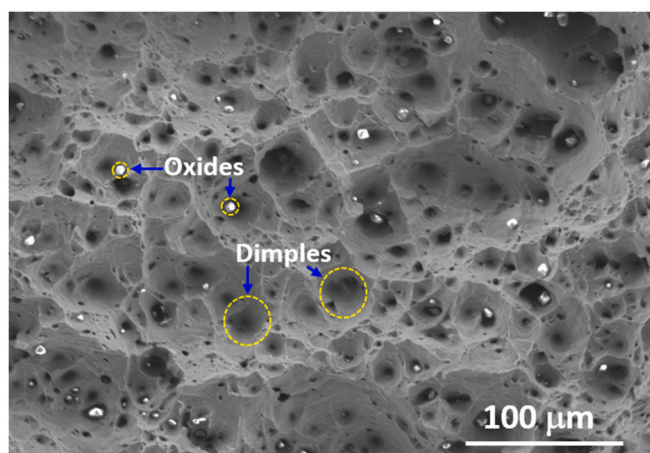
Fig. 21. Fracture surface of the CoCrFeMnNi gas metal arc welded joint with ER410-NiMo filler.

calculations, X-ray synchrotron diffraction and mechanical testing, a connection between the microstructure and mechanical properties of the welded joints is established. The following main conclusions were drawn:

1) A gas metal arc welded joint of CoCrFeMnNi high entropy alloy using ER410-NiMo stainless steel filler wire was successfully obtained without welding defects.
2) The thermal cycle influenced the recrystallization and grain growth phenomena experienced in the HAZ, promoting different softening effects (in terms of magnitude). In particular, in the low temperature HAZ there was only a moderate decrease in hardness, whereas in the high temperature HAZ an abrupt decay was observed. The composition change of the FZ was not conducive to a solid solution strengthening effect.
3) High energy synchrotron X-ray diffraction was used to determine the phase constituents within the FZ, while thermodynamic simulations were employed to predict the effect of different dilution ratios. A good agreement was obtained when considering C as a fast diffuser in the Scheil-Gulliver calculations.
4) Analysis of the FWHM evolution analysis along the joints revealed that the actual extension of the HAZ is slightly larger than that obtained considering both electron microscopy and microhardness measurements. This is due to recovery of the heavily cold rolled BM which occurs in the low temperature HAZ.
5) The gas metal arc welded CoCrFeMnNi joints with ER410-NiMo filler wire exhibited an increase in tensile strength (641 vs 519 MPa) but a slight decrease in elongation (7.3 vs 9.5%) compared to gas tungsten arc welded CoCrFeMnNi joints without the addition of filler wire. The good strength and ductility of these joints open the door for the potential application of gas metal arc welding of CoCrFeMnNi high entropy alloys for industrial-oriented applications.
6) Non-contact digital image correlation was used to obtain local stress-strain curves for different regions of the joint, confirming the existence of preferential strain concentrations at the weld toe interface site where fracture initiates. The local mechanical response is in good agreement with microstructure features observed across the welded joint.

The raw/processed data required to reproduce these findings cannot be shared at this time as the data also forms part of an ongoing study.

CRediT authorship contribution statement

Jiajia Shen: Formal analysis, Data curation, Methodology,

Investigation, Writing - original draft. **Rita Gonçalves:** Formal analysis, Data curation, Investigation. **Yeon Taek Choi:** Data curation, Investigation. **J.G. Lopes:** Investigation. **Jin Yang:** Investigation. **N. Schell:** Resources. **Hyoung Seop Kim:** Resources, Formal analysis. **J.P. Oliveira:** Resources, Validation, Conceptualization, Methodology, Formal analysis.

Declaration of competing interest

The authors declare that they have no known competing financial interests or personal relationships that could have appeared to influence the work reported in this paper.

Data availability

Data will be made available on request.

Acknowledgments

References

[1] B. Cantor, I.T.H. Chang, P. Knight, A.J.B. Vincent, Microstructural development in equiatomic multicomponent alloys, Mater. Sci. Eng., A 375–377 (2004) 213–218, https://doi.org/10.1016/j.msea.2003.10.257.
[2] J.-W. Yeh, S.-K. Chen, S.-J. Lin, J.-Y. Gan, T. Chin, T.-T. Shun, C. Tsau, S.-Y. Chang, Nanostructured high-entropy alloys with multiple principal elements: novel alloy design concepts and outcomes, Adv. Eng. Mater. 6 (2004) 299–303, https://doi.org/10.1002/adem.200300567.
[3] K.-Y. Tsai, M.-H. Tsai, J.-W. Yeh, Sluggish diffusion in Co–Cr–Fe–Mn–Ni high-entropy alloys, Acta Mater. 61 (2013) 4887–4897, https://doi.org/10.1016/j.actamat.2013.04.058.
[4] C. Lee, Y. Chou, G. Kim, M.C. Gao, K. An, J. Brechtl, C. Zhang, W. Chen, J. D. Poplawsky, G. Song, Y. Ren, Y. Chou, P.K. Liaw, Lattice-distortion-Enhanced yield strength in a refractory high-entropy alloy, Adv. Mater. 32 (2020), 2004029, https://doi.org/10.1002/adma.202004029.
[5] A. Raza, H.J. Ryu, S.H. Hong, Strength enhancement and density reduction by the addition of Al in CrFeMoV based high-entropy alloy fabricated through powder metallurgy, Mater. Des. 157 (2018) 97–104, https://doi.org/10.1016/j.matdes.2018.07.023.
[6] M. Seifi, D. Li, Z. Yong, P.K. Liaw, J.J. Lewandowski, Fracture toughness and fatigue crack growth behavior of as-cast high-entropy alloys, JOM 67 (2015) 2288–2295, https://doi.org/10.1007/s11837-015-1563-9.
[7] Y. Shi, B. Yang, P. Liaw, Corrosion-Resistant high-entropy alloys: a review, Metals 7 (2017) 43, https://doi.org/10.3390/met7020043.
[8] K. Lu, A. Chauhan, D. Litvinov, A.S. Tirunilai, J. Freudenberger, A. Kauffmann, M. Heilmaier, J. Aktaa, Micro-mechanical deformation behavior of CoCrFeMnNi high-entropy alloy, J. Mater. Sci. Technol. 100 (2022) 237–245, https://doi.org/10.1016/j.jmst.2021.04.079.
[9] F.C. Garcia Filho, S.N. Monteiro, Welding joints in high entropy alloys: a short-review on recent trends, Materials 13 (2020) 1411, https://doi.org/10.3390/ma13061411.
[10] Z. Wu, S.A. David, Z. Feng, H. Bei, Weldability of a high entropy CrMnFeCoNi alloy, Scripta Mater. 124 (2016) 81–85, https://doi.org/10.1016/j.scriptamat.2016.06.046.
[11] M.-G. Jo, H.-J. Kim, M. Kang, P.P. Madakashira, E.S. Park, J.-Y. Suh, D.-I. Kim, S.-T. Hong, H.N. Han, Microstructure and mechanical properties of friction stir

welded and laser welded high entropy alloy CrMnFeCoNi, Met. Mater. Int. 24 (2018) 73–83, https://doi.org/10.1007/s12540-017-7248-x.

[12] N. Kashaev, V. Ventzke, N. Stepanov, D. Shaysultanov, V. Sanin, S. Zherebtsov, Laser beam welding of a CoCrFeNiMn-type high entropy alloy produced by self-propagating high-temperature synthesis, Intermetallics 96 (2018) 63–71, https://doi.org/10.1016/j.intermet.2018.02.014.

[13] H. Nam, C. Park, C. Kim, H. Kim, N. Kang, Effect of post weld heat treatment on weldability of high entropy alloy welds, Sci. Technol. Weld. Join. 23 (2018) 420–427, https://doi.org/10.1080/13621718.2017.1405564.

[14] Z. Wu, S.A. David, Z. Feng, H. Bei, Weldability of a high entropy CrMnFeCoNi alloy, Scripta Mater. 124 (2016) 81–85, https://doi.org/10.1016/j.scriptamat.2016.06.046.

[15] Y. Hu, Y. Niu, Y. Zhao, W. Yang, X. Ma, J. Li, Friction stir welding of CoCrNi medium-entropy alloy: recrystallization behaviour and strengthening mechanism, Mater. Sci. Eng. 848 (2022) 143361, https://doi.org/10.1016/j.msea.2022.143361.

[16] Y. Lu, X. Zhang, H. Wang, C. Kan, F. Zhang, P. Dai, H. Wang, Investigation of microstructure, texture, and mechanical properties of FeCoNiCrMn high entropy alloy during drive friction welding, Mater. Char. 189 (2022) 111959, https://doi.org/10.1016/j.matchar.2022.111959.

[17] S.S. Nene, K. Liu, M. Frank, R.S. Mishra, R.E. Brennan, K.C. Cho, Z. Li, D. Raabe, Enhanced strength and ductility in a friction stir processing engineered dual phase high entropy alloy, Sci. Rep. 7 (2017), 16167, https://doi.org/10.1038/s41598-017-16509-9.

[18] J.-Y. Lin, Z.-H. Lai, T. Otsuki, H.-W. Yen, S. Nambu, Gradient microstructure and interfacial strength of CoCrFeMnNi high-entropy alloy in solid-state ultrasonic welding, Mater. Sci. Eng. 825 (2021), 141885, https://doi.org/10.1016/j.msea.2021.141885.

[19] N.K. Adomako, G. Shin, N. Park, K. Park, J.H. Kim, Laser dissimilar welding of CoCrFeMnNi-high entropy alloy and duplex stainless steel, J. Mater. Sci. Technol. 85 (2021) 95–105, https://doi.org/10.1016/j.jmst.2021.02.003.

[20] H. Do, S. Asadi, N. Park, Microstructural and mechanical properties of dissimilar friction stir welded CoCrFeMnNi high entropy alloy to STS304 stainless steel, Mater. Sci. Eng. 840 (2022), 142979, https://doi.org/10.1016/j.msea.2022.142979.

[21] K. Maeda, A. Niitsu, H. Morito, K. Shiga, K. Fujiwara, In situ observation of grain boundary groove at the crystal/melt interface in Cu, Scripta Mater. 146 (2018) 169–172, https://doi.org/10.1016/j.scriptamat.2017.11.039.

[22] H. Nam, B. Moon, S. Park, N. Kim, S. Song, N. Park, Y. Na, N. Kang, Gas tungsten arc weldability of stainless steel 304 using CoCrFeMnNi filler metals for cryogenic applications, Sci. Technol. Weld. Join. 27 (2022) 33–42, https://doi.org/10.1080/13621718.2021.1996851.

[23] H. Nam, B. Moon, S. Park, N. Kim, S. Song, N. Park, Gas tungsten arc weldability of stainless steel 304 using CoCrFeMnNi filler metals for cryogenic applications, Sci. Technol. Weld. Join. 27 (2022) 33–42, https://doi.org/10.1080/13621718.2021.1996851.

[24] H. Nam, S. Park, N. Park, Y. Na, H. Kim, S.-J. Yoo, Y.-H. Moon, N. Kang, Weldability of cast CoCrFeMnNi high-entropy alloys using various filler metals for cryogenic applications, J. Alloys Compd. 819 (2020) 153278, https://doi.org/10.1016/j.jallcom.2019.153278.

[25] H. Nam, S. Yoo, J.W. Ha, B. Lee, S. Song, Y. Na, N. Kang, Enhancement of tensile properties of gas tungsten arc welds using Cu-coated CoCrFeMnNi filler and post–weld heat treatment, J. Mater. Res. Technol. 19 (2022) 4857–4866, https://doi.org/10.1016/j.jmrt.2022.07.023.

[26] H. Nam, S. Yoo, J. Lee, Y. Na, N. Park, N. Kang, GTA weldability of rolled high-entropy alloys using various filler metals, Metals 10 (2020) 1371, https://doi.org/10.3390/met10101371.

[27] J.P. Oliveira, A. Shamsolhodaei, J. Shen, J.G. Lopes, R.M. Gonçalves, M. de Brito Ferraz, L. Piçarra, Z. Zeng, N. Schell, N. Zhou, H. Seop Kim, Improving the ductility in laser welded joints of CoCrFeMnNi high entropy alloy to 316 stainless steel, Mater. Des. 219 (2022) 110717, https://doi.org/10.1016/j.matdes.2022.110717.

[28] J.P. Oliveira, A. Shamsolhodaei, J. Shen, J.G. Lopes, R.M. Gonçalves, M. de Brito Ferraz, L. Piçarra, Z. Zeng, N. Schell, N. Zhou, H. Seop Kim, Improving the ductility in laser welded joints of CoCrFeMnNi high entropy alloy to 316 stainless steel, Mater. Des. 219 (2022) 110717, https://doi.org/10.1016/j.matdes.2022.110717.

[29] J.P. Oliveira, J. Shen, Z. Zeng, J.M. Park, Y.T. Choi, N. Schell, E. Maawad, N. Zhou, H.S. Kim, Dissimilar laser welding of a CoCrFeMnNi high entropy alloy to 316 stainless steel, Scripta Mater. 206 (2022), 114219, https://doi.org/10.1016/j.scriptamat.2021.114219.

[30] N.K. Adomako, G. Shin, N. Park, K. Park, J.H. Kim, Laser dissimilar welding of CoCrFeMnNi-high entropy alloy and duplex stainless steel, J. Mater. Sci. Technol. 85 (2021) 95–105, https://doi.org/10.1016/j.jmst.2021.02.003.

[31] H. Do, S. Asadi, N. Park, Microstructural and mechanical properties of dissimilar friction stir welded CoCrFeMnNi high entropy alloy to STS304 stainless steel, Mater. Sci. Eng. 840 (2022), 142979, https://doi.org/10.1016/j.msea.2022.142979.

[32] H. Nam, S. Park, S.H. Shim, Y.-S. Na, N. Kim, S. Song, S.I. Hong, N. Kang, Enhancement of tensile properties applying phase separation with Cu addition in gas tungsten arc welds of CoCrFeMnNi high entropy alloys, SSRN Electron. J. 220 (2022), 114897, https://doi.org/10.2139/ssrn.4044644.

[33] J.P. Oliveira, T.M. Curado, Z. Zeng, J.G. Lopes, E. Rossinyol, J.M. Park, N. Schell, F. M. Braz Fernandes, H.S. Kim, Gas tungsten arc welding of as-rolled CrMnFeCoNi high entropy alloy, Mater. Des. 189 (2020), 108505, https://doi.org/10.1016/j.matdes.2020.108505.

[34] J.P. Oliveira, J. Shen, J.D. Escobar, C.A.F. Salvador, N. Schell, N. Zhou, O. Benafan, Laser welding of H-phase strengthened Ni-rich NiTi-20Zr high temperature shape memory alloy, Mater. Des. 202 (2021), 109533, https://doi.org/10.1016/j.matdes.2021.109533.

[35] A.P. Hammersley, S.O. Svensson, M. Hanfland, A.N. Fitch, D. Hausermann, Two-dimensional detector software: from real detector to idealised image or two-theta scan, High Pres. Res. 14 (1996) 235–248, https://doi.org/10.1080/08957959608201408.

[36] B.H. Toby, R.B. Von Dreele, GSAS-II : the genesis of a modern open-source all purpose crystallography software package, J. Appl. Crystallogr. 46 (2013) 544–549, https://doi.org/10.1107/S0021889813003531.

[37] L. Lutterotti, R. Vasin, H.-R. Wenk, Rietveld texture analysis from synchrotron diffraction images. I. Calibration and basic analysis, Powder Diffr. 29 (2014) 76–84, https://doi.org/10.1017/S0885715613001346.

[38] F. Galbusera, A.G. Demir, J. Platl, C. Turk, R. Schnitzer, B. Previtali, Processability and cracking behaviour of novel high-alloyed tool steels processed by Laser Powder Bed Fusion, J. Mater. Process. Technol. 302 (2022), 117435, https://doi.org/10.1016/j.jmatprotec.2021.117435.

[39] M. Ma, R. Lai, J. Qin, B. Wang, H. Liu, D. Yi, Effect of weld reinforcement on tensile and fatigue properties of 5083 aluminum metal inert gas (MIG) welded joint: experiments and numerical simulations, Int. J. Fatig. 144 (2021), 106046, https://doi.org/10.1016/j.ijfatigue.2020.106046.

[40] A. Singh, D.A. Basha, Y. Matsushita, K. Tsuchiya, Z. Lu, T.-G. Nieh, T. Mukai, Domain structure and lattice effects in a severely plastically deformed CoCrFeMnNi high entropy alloy, J. Alloys Compd. 812 (2020), 152028, https://doi.org/10.1016/j.jallcom.2019.152028.

[41] X. Ma, J. Chen, X. Wang, Y. Xu, Y. Xue, Microstructure and mechanical properties of cold drawing CoCrFeMnNi high entropy alloy, J. Alloys Compd. 795 (2019) 45–53, https://doi.org/10.1016/j.jallcom.2019.04.296.

[42] Z. Zhu, X. Ma, C. Wang, G. Mi, S. Zheng, The metallurgical behaviors and crystallographic characteristic on macro deformation mechanism of 316 L laser-MIG hybrid welded joint, Mater. Des. 194 (2020), 108893, https://doi.org/10.1016/j.matdes.2020.108893.

[43] X.-M. Chen, Y.C. Lin, F. Wu, EBSD study of grain growth behavior and annealing twin evolution after full recrystallization in a nickel-based superalloy, J. Alloys Compd. 724 (2017) 198–207, https://doi.org/10.1016/j.jallcom.2017.07.027.

[44] W.L. Grube, S.R. Rouze, The origin, growth and annihilation of annealing twins in austenite, Can. Metall. Q. 2 (1963) 31–52, https://doi.org/10.1179/cmq.1963.2.1.31.

[45] C. Wang, J. Yu, Y. Zhang, Y. Yu, Phase evolution and solidification cracking sensibility in laser remelting treatment of the plasma-sprayed CrMnFeCoNi high entropy alloy coating, Mater. Des. 182 (2019), 108040, https://doi.org/10.1016/j.matdes.2019.108040.

[46] C. Zhang, J. Zhu, C. Ji, Y. Guo, R. Fang, S. Mei, S. Liu, Laser powder bed fusion of high-entropy alloy particle-reinforced stainless steel with enhanced strength, ductility, and corrosion resistance, Mater. Des. 209 (2021), 109950, https://doi.org/10.1016/j.matdes.2021.109950.

[47] R. Sokkalingam, P. Mastanaiah, V. Muthupandi, K. Sivaprasad, K.G. Prashanth, Electron-beam welding of high-entropy alloy and stainless steel: microstructure and mechanical properties, Mater. Manuf. Process. 35 (2020) 1885–1894, https://doi.org/10.1080/10426914.2020.1802045.

[48] B. Gludovatz, A. Hohenwarter, D. Catoor, E.H. Chang, E.P. George, R.O. Ritchie, A fracture-resistant high-entropy alloy for cryogenic applications, Science 345 (2014) 1153–1158, https://doi.org/10.1126/science.1254581.

[49] Y.-K. Kim, Y.-A. Joo, H.S. Kim, K.-A. Lee, High temperature oxidation behavior of Cr-Mn-Fe-Co-Ni high entropy alloy, Intermetallics 98 (2018) 45–53, https://doi.org/10.1016/j.intermet.2018.04.006.

[50] J.P. Oliveira, D. Barbosa, F.M.B. Fernandes, R.M. Miranda, Tungsten inert gas (TIG) welding of Ni-rich NiTi plates: functional behavior, Smart Mater. Struct. 25 (2016), https://doi.org/10.1088/0964-1726/25/3/03LT01, 03LT01.

[51] H. Nam, S. Park, E.-J. Chun, H. Kim, Y. Na, N. Kang, Laser dissimilar weldability of cast and rolled CoCrFeMnNi high-entropy alloys for cryogenic applications, Sci. Technol. Weld. Join. 25 (2020) 127–134, https://doi.org/10.1080/13621718.2019.1644471.

[52] G. Qin, R. Chen, H. Zheng, H. Fang, L. Wang, Y. Su, J. Guo, H. Fu, Strengthening FCC-CoCrFeMnNi high entropy alloys by Mo addition, J. Mater. Sci. Technol. 35 (2019) 578–583, https://doi.org/10.1016/j.jmst.2018.10.009.

[53] A.J. Zaddach, C. Niu, C.C. Koch, D.L. Irving, Mechanical properties and stacking fault energies of NiFeCrMnCo high-entropy alloy, JOM 65 (2013) 1780–1789, https://doi.org/10.1007/s11837-013-0771-4.

[54] A.J. Zaddach, R.O. Scattergood, C.C. Koch, Tensile properties of low-stacking fault energy high-entropy alloys, Mater. Sci. Eng., A 636 (2015) 373–378, https://doi.org/10.1016/j.msea.2015.03.109.

[55] B. Li, Z. Qin, H. Xue, Z. Sun, T. Gao, Optimization of shot peening parameters for AA7B50-T7751 using response surface methodology, Simulat. Model. Pract. Theor. 115 (2022), 102426, https://doi.org/10.1016/j.simpat.2021.102426.

[56] N. Jia, Z.H. Cong, X. Sun, S. Cheng, Z.H. Nie, Y. Ren, P.K. Liaw, Y.D. Wang, An in situ high-energy X-ray diffraction study of micromechanical behavior of multiple phases in advanced high-strength steels, Acta Mater. 57 (2009) 3965–3977, https://doi.org/10.1016/j.actamat.2009.05.002.

[57] B. Nagarajan, D. Kumar, Z. Fan, S. Castagne, Effect of deep cold rolling on mechanical properties and microstructure of nickel-based superalloys, Mater. Sci. Eng., A 728 (2018) 196–207, https://doi.org/10.1016/j.msea.2018.05.005.

[58] Z. Cui, Y. Mi, D. Qiu, P. Dong, Z. Qin, D. Gong, W. Li, Microstructure and mechanical properties of additively manufactured CrMnFeCoNi high-entropy alloys after ultrasonic surface rolling process, J. Alloys Compd. 887 (2021), 161393, https://doi.org/10.1016/j.jallcom.2021.161393.

[59] J. Gu, M. Song, Annealing-induced abnormal hardening in a cold rolled CrMnFeCoNi high entropy alloy, Scripta Mater. 162 (2019) 345–349, https://doi.org/10.1016/j.scriptamat.2018.11.042.

[60] H.-Y. Huang, I.-C. Kuo, C.-W. Zhang, Friction-stir welding of aluminum alloy with an iron-based metal as reinforcing material, Sci. Eng. Compos. Mater. 25 (2018) 123–131, https://doi.org/10.1515/secm-2016-0065.

[61] A. Hasnaoui, H. Van Swygenhoven, P.M. Derlet, Dimples on nanocrystalline fracture surfaces as evidence for shear plane formation, Science 300 (2003) 1550–1552, https://doi.org/10.1126/science.1084284.